

Usman Zamir Afridi

Numerical Simulation of turbulent Flow Over a Cavity

Department of Applied Mechanics  
*Division of Fluid Dynamics*  
CHALMERS UNIVERSITY OF TECHNOLOGY  
Göteborg Sweden, 2012

Master's Thesis 2012 : 02



MASTER'S THESIS 2012:02

**Numerical Simulation of turbulent Flow Over  
a Cavity**

Master's Thesis

USMAN ZAMIR AFRIDI

Department of Applied Mechanics  
*Division of Fluid Dynamics*  
CHALMERS UNIVERSITY OF TECHNOLOGY  
Göteborg, Sweden, 2012

Numerical Simulation of turbulent Flow Over a Cavity  
Master's Thesis  
Usman Zamir Afridi

© USMAN ZAMIR AFRIDI, 2012

Master's Thesis 2012:02  
ISSN: 1652-8557

Department of Applied Mechanics,  
Division of Fluid Dynamics  
Chalmers University of Technology  
SE-412 96 Göteborg, Sweden  
Phone +46-(0)31-7721400  
Fax: +46-(0)31-180976

Printed at Chalmers Reproservice  
Göteborg, Sweden 2012

# Usman Zamir Afridi

Master's Thesis

by

Usman Zamir Afridi

usmanza@student.chalmers.se

Department of Applied Mechanics

Division of Fluid Dynamics

Chalmers University of Technology

## Abstract

Cavity flow and control of these flows have been of great importance for military as well as civil applications. Modern aircraft with internal carriage of weapon require active flow control techniques to ensure the structural integrity by limiting the open bay acoustic resonance and efficient payload deployment. To implement these techniques it is important to understand the flow features and identify the source of resonance. Detached Eddy Simulation (DES) is carried out for subsonic flow ( $M = 0.85$ ) over a three dimensional cavity with Reynolds number based of cavity length equal to  $7 \times 10^6$ . A good comparison with the available experimental data for the similar configuration validates the DES results. Special attention is paid towards the prediction of unsteady pressure fluctuations and mixing layer and the resulting tonal modes due to their interaction. Furthermore, the instantaneous and mean flow structures inside the cavity are compared with the available Large Eddy Simulation (LES) data, showing a good agreement with slight deviation at the leading edge of the cavity. The Sound Pressure Level (SPL) comparison on cavity floor points show a good match between DES and experimental results and also capturing the tonal modes. The Overall Sound Pressure (OASPL) distribution is slightly overestimated (with maximum difference equal to 1.5dB) by the DES. It is also observed that the self sustained oscillations related to the tonal modes are independent of the stream-wise location in the cavity. The correlation analysis of the cavity floor points reveal that the low frequencies are more correlated to the pressure fluctuations in these locations.

### Keywords:

Cavity flow, Detached Eddy Simulation (DES), Computational Fluid Dynamics (CFD), Sound Pressure Level (SPL), Aeroacoustics, correlation



## Acknowledgement

I would like to thank:

My supervisors, Professor Lars Davidson and Shia-Hui Peng, for their guidance and great support through their availability and dynamic discussions throughout this work. It was only their persistent support and patience that made it possible for me to carry out this work.

And, of course, all the people at the Department for their help and support especially Bestian Nebensfur for providing me a head start with the Edge and assistance in postprocessing the results by sharing tips and tricks. I would like to appreciate Huadong for taking me through the aeroacoustic part and Sebastian Arvidson for providing a deeper insight into the parallel processing and CFD methods in general and in Edge in particular.

Last but not the least I would like to thank my family for believing in me and making it possible for me to pursue my dream of higher education. I would especially thank my wife for her support and love during my thesis work.

I would like to express my gratitude to QinetiQ for their experimental data and Lionel Larcheveque for LES results for comparison.

# Nomenclature

## ***Upper-case Roman***

$C_{b1}, C_{b2}, C_{w1}$	Turbulence model constants
$C_p$	Specific heat at constant pressure
$C_v$	Specific heat at constant pressure
$M$	Mach Number
$P$	Pressure
$Pr$	Prandtl number
$R$	Gas constant
$Re$	Reynolds number
$S$	Local deformation rate
$S^*_{ij}$	Trace-less viscous strain
$T$	Temperature
$U$	Velocity
$(L, T, U)$	Length, width and height of cavity respectively

## ***Lower-case Roman***

$d$	Distance to the closest wall
$\tilde{d}$	Turbulent length scale
$e$	Internal energy
$e_o$	Total energy
$f_n$	Frequency (n <sup>th</sup> Rossiter Mode)
$f_{\nu 2}$	Wall damping functions
$k$	Turbulent kinetic energy
$n$	Number of mode
$u_i$	Cartesian components of velocity vector
$x_i$	Cartesian coordinate vector component
$p$	Pressure
$q$	Heat flux
$t$	Time
$y$	Distance to the wall

## ***Upper-case Greek***

$\Delta t$	Time step size
$\Delta x, \Delta y, \Delta z$	Streamwise, normal and spanwise mesh spacings

$\Omega$  Mean vorticity tensor

***Lower-case Greek***

$\delta$  Turbulent inflow boundary layer thickness  
 $\gamma$  Empirical constant in Rossiter Formula  
 $\kappa$  Von Karman constant, empirical constant in Rossiter formula  
 $\lambda$  Thermal diffusion rate  
 $\mu$  Dynamic viscosity  
 $\tilde{\nu}$  Kinematic eddy viscosity parameter  
 $\rho$  Density  
 $\tau_{ij}$  Viscous stress tensor  
 $\tau_w$  Wall shear stress

***Abbreviations***

BISPL Band Integrated Sound Pressure Level  
BL Boundary Layer  
CFD Computational Fluid Dynamics  
CFL Courant, Friedrichs and Lewy number  
DES Detached Eddy Simulation  
DHIT Decaying Homogenous Isotropic Turbulence  
DNS Direct Numerical Simulation  
EARSM Explicit Algebraic Reynolds Stress Model  
OASPL Overall Sound Pressure Level  
PSD Power Spectrun Density  
RANS Reynolds-averaged Navier-Stokes  
SA Spalart Allmaras (model)  
SGS Sub-Grid-Scale  
SPL Sound Pressure Level  
SST Shear Stress Transport  
URANS Unsteady Reynolds-averaged Navier-Stokes

***subscripts***

$\delta$  Quantity based on half channel-width  
 $i$  Direction, node number  
 $ij$  Tensor indices  
 $\infty$  Freestream

***superscripts***

$\sim$	Ensemble average quantity
$\tilde{\cdot}$	Favre-filtered ensemble average quantity
$'$	Fluctuating component (Reynolds averaging)
$''$	Fluctuating component (Favre averaging)
$y^+$	$=y_p u^* / \nu$

# Contents

<b>Abstract</b>	<b>5</b>
<b>Acknowledgement</b>	<b>7</b>
<b>Nomenclature</b>	<b>8</b>
<b>1 Introduction</b>	<b>1</b>
1.1 Purpose . . . . .	2
1.2 Limitations . . . . .	2
<b>2 Cavity Flow</b>	<b>5</b>
2.1 Introduction . . . . .	5
2.2 Noise Generation . . . . .	5
2.3 Classification of cavity . . . . .	6
2.3.1 Classification based on $L/D$ . . . . .	6
2.3.2 Classification based on $L/W$ . . . . .	7
2.3.3 Classification based on flow phenomenon . . . . .	7
2.4 Cavity Flow Properties . . . . .	10
2.4.1 Mach Number Effects . . . . .	11
2.4.2 Boundary Layer Thickness ( $L/\delta$ ) . . . . .	11
2.4.3 Pressure Spectra . . . . .	11
2.4.4 Rossiter Modes . . . . .	12
<b>3 Turbulence Modeling</b>	<b>15</b>
3.1 Introduction . . . . .	15
3.2 Governing Equation . . . . .	15
3.2.1 Fluid Modeling . . . . .	17
3.2.2 Time average Navier Stokes . . . . .	17
3.3 Turbulence Models . . . . .	18
3.3.1 Close Form of Favre average Navier Stokes . . . . .	19
3.3.2 Spalart Allmaras One-equation model . . . . .	22

3.3.3	Wilcox Standard $k - \omega$ turbulence model . . . . .	23
3.3.4	SST Menter $k - \omega$ turbulence model . . . . .	24
3.3.5	Explicit Algebraic Reynolds Stress Models (EARSM) . . . . .	25
3.4	Spalart-Allmaras DES Model . . . . .	28
<b>4</b>	<b>Simulation Methods</b>	<b>29</b>
4.1	The Unstructured CFD Solver Edge . . . . .	29
4.1.1	Geometrical Considerations . . . . .	30
4.2	Boundary Condition . . . . .	31
4.2.1	Wall Boundary Condition . . . . .	32
4.2.2	Symmetry Condition . . . . .	33
4.2.3	Farfield (Weak Characteristic) . . . . .	33
4.3	Running a Computation With Edge . . . . .	33
4.3.1	Edge Files . . . . .	33
4.3.2	Grid . . . . .	34
4.3.3	Edge Parameters . . . . .	34
4.3.4	Numerical Scheme . . . . .	34
4.3.5	Boundary conditions . . . . .	35
4.3.6	Time Integration . . . . .	35
4.4	The Computational Set-up . . . . .	35
<b>5</b>	<b>Results and Discussion</b>	<b>39</b>
5.1	2D Results . . . . .	39
5.1.1	Computational setup . . . . .	39
5.1.2	Summary of Results . . . . .	40
5.2	3D Results . . . . .	41
5.2.1	Mean Flow Comparison . . . . .	41
5.2.2	Pressure Oscillations . . . . .	45
5.2.3	Pressure Correlations . . . . .	48
<b>6</b>	<b>Conclusion and Outlook</b>	<b>57</b>
6.1	Conclusion and Outlook . . . . .	57

# Chapter 1

## Introduction

Cavity flows phenomenon have been of great interest in a variety of engineering applications, which can be observed, for example in the landing-gear well in the deployment at landing and takeoff of aircraft, weapon bay of fighters, window open conditions in automobile industry, separation between two consecutive bogies of trains and depressions in hull of ships and sub-marines.

Cavity flows in aeronautic applications have been extensively studied both experimentally and computationally. With the purpose of reducing the radar visibility and improve the aerodynamic performance. In addition, cavity flow resulting from landing-gear box during takeoff and landing has been regarded as being one of the major contributors of airframe noise due to extensive pressure fluctuations. Along with that, extensive pressure fluctuations may further lead to structural fatigue and damaging the structure and the avionics housed in the cavity.

Apart from the importance of the cavity flow in a variety of applications, the sophisticated flow physics of cavity flows has always attracted people to study it. The Study by Roshko [1] was one of the pioneering work. The main focus was laid on the strong self-sustained oscillations that arise from the vorticity-pressure feedback loop encountered in this kind of flow. Flow inside cavities is distinguished by boundary layer separation, shear layer instabilities, unsteadiness and vortical flow motion. Due to these flow features, the cavity flow is prone to aero-acoustic resonance. The acoustic tones generated are often regarded as a result of interaction between shear layer and the aft wall on which it impinges [2]. Another major contribution to cavity flow study is the formula proposed by Rossiter[3]. The resonant loop of mixing-layer vortices moving downstream with velocity  $\kappa U_\infty$  and pressure waves traveling upstream inside the cavity with the speed of sound, results in discrete tonal modes, of which the frequency can be approximately calculated by using the Rossiter formula (Eq. 2.1).

The present study concerns of numerical simulations of a generic configuration weapon-bay. The rectangular cavity has the dimensions of  $L = 20$  inches in length,  $D = 4$  inches in diameter and  $W = 4$  inches in width, giving an aspect ratio of  $L : D : W = 4 : 1 : 1$ . The cavity was analyzed with freestream flow conditions of  $M_\infty = 0.85$ ,  $P_\infty = 6.21 \times 10^4$ ,  $T_\infty = 266.53K$  and  $Re = 13.47 \times 10^6$  per meter.

## 1.1 Purpose

The purpose of this project is to explain the cavity flow physics by means of accurate flow simulations and to understand how these simulations can be improved for solving cavity flows. The main focus is laid on resolving the complex flow structures, prediction of pressure fluctuations and the generated acoustic tones inside the cavity. Furthermore, to add to the available database of extensive work already carried out over the *M219 – cavity* in a previous EU DESider project [4]. This will be useful in examination of turbulence modeling of this kind of flows. Based on the simulation, another important objective is to interpret the interaction of acoustic tones with the shear layer instabilities. It is expected the analysis may provide implications for future work on flow control of cavity flows.

## 1.2 Limitations

With turbulence resolving simulations using DES and other hybrid RANS-LES methods, the requirement on computational resources is further high. The DES computation carried out was computationally heavy requiring long time to run, therefore, there was little flexibility in trying different settings/turbulence models. Also the data storage required to store the flow solution at each timestep for entire domain further increases the simulation time, which might have been helpful in analyzing shear layer region more extensively with a better insight to flow behavior in that particular region.

The computation started with 2D simulations using RANS. It was found that the Spalart-Allmaras and EARSM model showed acceptable convergence, whereas for the Menter SST  $k - \omega$  and the Wilcox Standard  $k - \omega$  turbulence model the simulation diverged. For URANS computations were also showing divergence using the SST  $k - \omega$  model. For the SA and the EARSM turbulence model, the unsteadiness in the flow was dampened out and the solution converges to a steady state.

With turbulence resolving simulations using DES and other hybrid RANS-LES methods, the requirement on computational resources is further high.



# Chapter 2

## Cavity Flow

### 2.1 Introduction

Cavity flow can be described as the interaction of different flow phenomenon, such as hydrodynamic instabilities, flow separation and recirculation, vortex motions, acoustic noise generation and wave propagation and aero-acoustic coupling related to the self-sustaining vorticity pressure feedback. The aero-acoustic resonance is the aerodynamic noise generated and the flow conditions in the cavity result in self sustaining oscillations, which have adverse affects on the integrity of the structure. In order to reduce the noise, it is important to understand the flow features and thus develop methods to control the flow. Cavity flow has been studied experimentally and numerically.

### 2.2 Noise Generation

One of the first researchers who carried out experimental work on cavity flow was Rossiter[3]. In his experiments he tested different geometries and by studying the shadowgraphs, identifying the pressure waves and flow pattern he came up with the description of the feedback mechanism. The source for the aerodynamic loads is due to the natural flow instabilities in the cavity. The shear layer develops as the freestream flow separates from the leading edge of the cavity. The shear layer breaks down further downstream, and the emerging vortex shedding impinging on the rear wall results in pressure waves. These pressure waves travel upstream and interact with the mixing layer. This interaction of the pressure wave with the Kelvin-Helmoltz type shear layer instability leads to a self sustained mechanism, inducing acoustic noise as shown schematically in Fig. 2.1. This process forms a feed back loop

and, upon the cavity geometry, tonal noise may generate due to unsteady pressure modes.

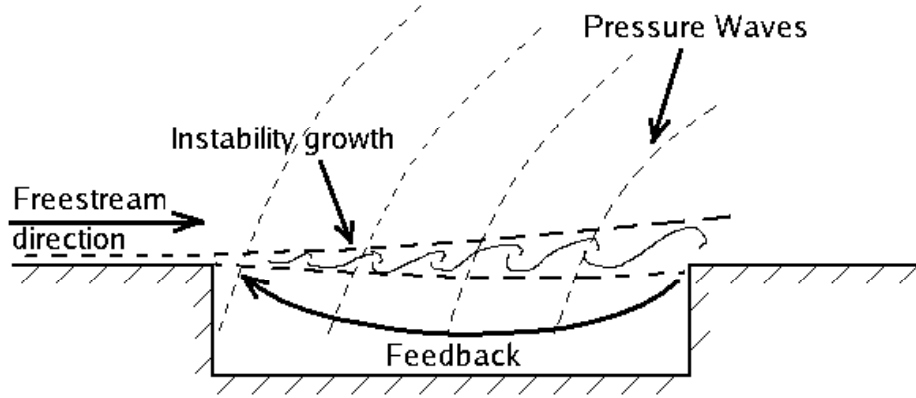


Figure 2.1: Schematic view of the self-sustained pressure oscillations

## 2.3 Classification of cavity

Depending upon the applications different kinds of cavities are used, which are classified on the basis of cavity geometry and the flow condition. Much experimental and numerical work have been carried out to study the affects of different geometries [3] [5] [6] and to identify different types of flow patterns in the cavity [7] [8] [9]. Some of the basic classifications are described below.

### 2.3.1 Classification based on $L/D$

One of the basic classification of cavities is deep and shallow cavities, based upon the aspect ratio ( $L/D$ ), where  $L$  and  $D$  are the characteristic length and depth of the cavity respectively. Cavities with aspect ratio smaller than one are categorized as deep cavities, whereas the one with aspect ratio larger than one are referred to as shallow cavities. On the other hand, Rossiter through his experimental observations described cavities with  $L/D < 4$  as deep cavities and vice versa. The deep cavities are associated with periodic and energetic tones, while in shallow cavities broadband noise (i.e. the random components) with higher amplitudes are generated.

### 2.3.2 Classification based on $L/W$

Several researchers have been analyzing the flow properties in the cavity under the influence of varying dimensions. Cavity with  $L/W < 1$  is referred as three-dimensional and if  $L/W > 1$  it is classified as two-dimensional. Block [10] was the first who classified the cavity on the basis of length-to-width ratio ( $L/W$ ). Ahuja and Mendoza [6] came up with the similar observations/results. They found that the frequency of the peak is unaffected by the change in cavity width, but there is approximately 15  $dB$  reduction in overall sound pressure level (OASPL) for 3D cavities. Furthermore, Dismile [5] observed that the number of tones of dominant frequencies increases as  $L/W$  decreases.

### 2.3.3 Classification based on flow phenomenon

Several factors involved in cavity flow may significantly impact the cavity flow properties. These include geometric variables like  $L/W$ ,  $L/D$  and flow parameters like free-stream Mach number. Based on the flow features, cavity flows have usually been classified into three different types, namely, Open, closed and transitional flow.

#### Closed flow

As shown in Fig. 2.2, a closed cavity flow is formed in case of cavity length-to-depth ratio larger than 13 [7]. In this type of flow the shear layer growing from the leading edge of the cavity impinges on the cavity floor, detaches further downstream from the cavity floor and finally passes over the cavity rear wall, resulting in two recirculation regions in the front and rear part of the cavity, one before the flow impinges on the cavity floor and the second one after the detachment, as shown in Fig. 2.2.

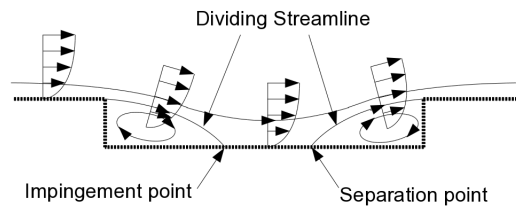


Figure 2.2: Sub-sonic closed cavity flow

For a closed cavity flow at supersonic conditions, an expansion wave is observed at the front wall and rear wall, where the flow turns away from itself

around the corner. A shock is generated at the location of flow attachment and detachment from the cavity floor, as illustrated in Fig. 2.3. The  $C_p$  behavior resulting from the expansion and shock waves is shown in Fig. 2.3.

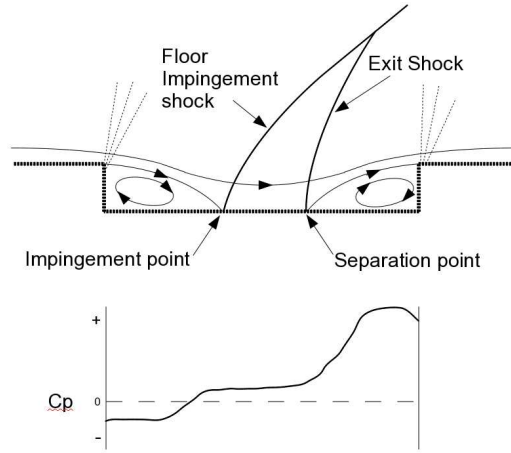


Figure 2.3: Super-sonic closed cavity flow with pressure distribution on cavity floor

## Open Flow

Open flow phenomenon is observed in the cavity with the length-to-depth ratio less than 10.[11]. In this case the shear layer does not impinge on the cavity floor and  $C_p$  exhibits a rather constant behavior except close to rear wall where the shear layer impinges. The open cavity flow pattern is shown in Fig. 2.4.

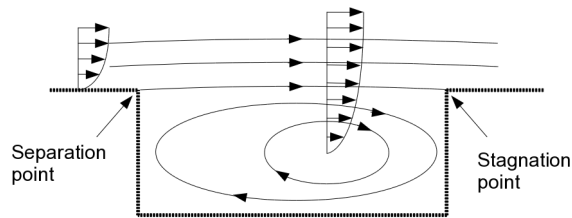


Figure 2.4: Sub-sonic open cavity flow

For open flows in supersonics conditions, an oblique shock appears at the leading edge and trailing edge of the cavity as shown in Fig. 2.5. The open cavities are associated with discrete tones with high acoustic intensity. An open cavity flow condition (with relatively uniform pressure distribution)

provides favorable conditions for cargo separation for weapon-bay type cavity [7].

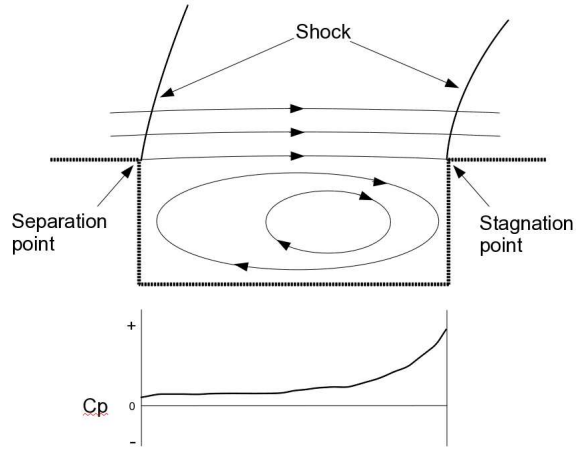


Figure 2.5: Super-sonic open cavity flow with pressure distribution on cavity floor

### Transitional flow

The cavity is said to be open when the reattachment of the shear layer takes place at the rear edge and in case of reattachment point on the cavity floor, it is called closed cavity. When the two states occur randomly, the flow is called transitional. This kind of behavior is observed in cavities with the length-to-depth ratio of  $10 < L/D < 13$  [11]. The transitional flow features are strongly dependent on the free-stream Mach number. For subsonic flow conditions the transition is a smooth process. At supersonic flow conditions it is a two-step process with abrupt changes in flow characteristics. The two stages are classified further as transitional open and transitional closed cavities based on the location of attached and detached shocks.

The supersonic transition from closed to open flow is illustrated in Fig. 2.3.3. In Fig. 2.6(a) the closed flow is observed with the expansion waves at leading and trailing edges of the cavity respectively, at impingement and detachment regions. When the length-to-width ratio is decreased the two shocks come closer, resulting in the first transitional stage called the transitional closed cavity, with a single shock, which is illustrated in Fig. 2.6(b). If the length-to depth ratio is further reduced the shear layer separated from the cavity floor result in a series of expansion and compression wavelets (as shown in Fig. 2.6(c)) known as transitional open cavity. Further reduction of length-to-depth will result in open cavity as shown in Fig. 2.6(d).

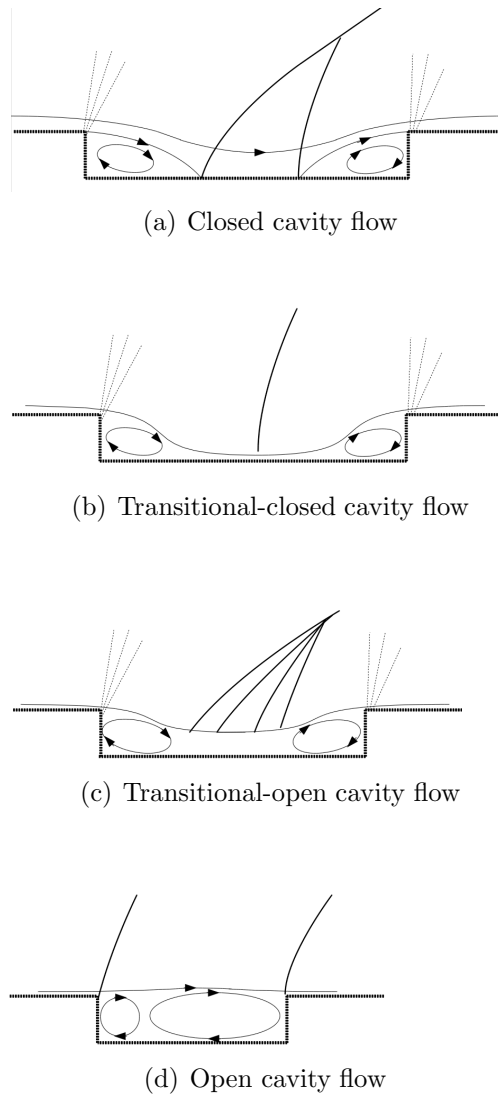


Figure 2.6: Transition of cavity flow from closed flow to open flow

## 2.4 Cavity Flow Properties

The behavior of flow inside the cavity in association with acoustic phenomena depends upon several flow parameters. Experiments show that the 'Mach number' and  $L/\delta$  (where,  $\delta$  is the turbulent inflow boundary layer (B.L) thickness) are of the major concerns since they have strong influence on the interaction of the shear layer instabilities and the acoustic tonal modes.

### 2.4.1 Mach Number Effects

Acoustic tones inside a cavity activate when a certain Mach number is achieved. With an increasing mach number, the cavity flow transits from the shear layer mode to wake mode. In shear layer mode, the dominant frequency of the pressure fluctuations seems to oscillate with increasing Mach number. Colonious et al. [12] by means of analysis of the Direct Numerical Simulation (DNS) data, observed that for the range of  $Mach = 0.4$  to  $0.8$ , the fundamental frequencies are almost independent of the Mach number. The experimental study by Gates et al. [13] further certified that the modal amplitude is independent of the Mach number.

### 2.4.2 Boundary Layer Thickness ( $L/\delta$ )

Incoming boundary layer thickness plays an important role in the cavity flow mechanism. Generally the boundary layer thickness is used to normalize the characteristic lengths (in this case length and depth of the cavity) for analysis and comparison, usually with  $L/\delta$  or  $D/\delta$ . Sarohia and Massiar [14] in their studies of the boundary layer effect observed that there exists a critical  $L/\delta$  value at which steady shear layer transits to unsteady shear layer. Rockwell and Nadascher [15] also observed a similar phenomenon and indicated a critical value of  $L/\delta$  beyond which a sudden increase occurs in the dominant frequencies, similar to the effect of Mach number in shear-layer mode.

### 2.4.3 Pressure Spectra

The sound waves travel as pressure waves generated by the unsteady flow field. The generation and propagation of these acoustic waves have always been of interest in aeronautic and other industrial applications. The governing equations for the aeroacoustic wave generation and propagation are the same as a fluid dynamics. One of the main problems while using the fluid dynamics equations is that the sound waves carry a very low energy as compared to the fluid flow itself. Therefore, resolving these sound waves numerically and predicting the propagation is quite a challenge. A typical pressure spectrum for unsteady cavity flow comprises of random and periodic pressure fluctuations, which vary in magnitude depending upon the type of flow. In case of closed cavity, the pressure spectrum is dominated by random pressure fluctuations. On the other hand, the open cavity flow is dominated by periodic pressure oscillations with less random fluctuations. A typical SPL spectra for open and closed cavity flow are shown in Fig. 2.7.

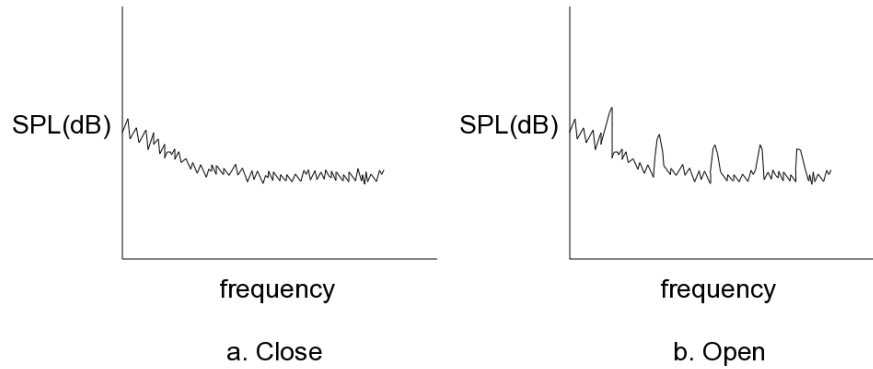


Figure 2.7: Typical Spectra of Open and Closed Cavity (random data)

Transitional cavity is similar to the open cavity flow with the periodic fluctuations, resulting in acoustic tones as shown in Fig. 2.7 (b).

### 2.4.4 Rossiter Modes

Discrete tones generation in cavity flow is associated with the interaction of the acoustic tones traveling upstream with the shear layer instabilities. This interaction is more obvious in open cavities and can be identified in the energy spectrum as peaks corresponding to respective frequencies. The magnitude of each peak is measured in terms of Sound Pressure Level (SPL), as shown in Fig. 2.8.

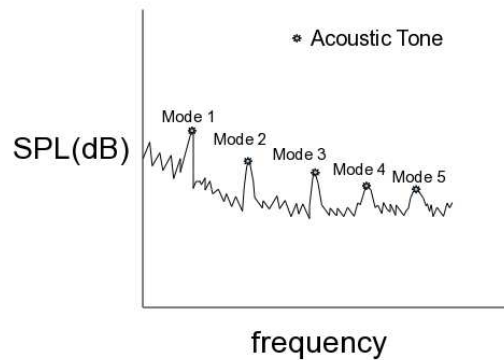


Figure 2.8: Rossiter modes in a spectrum (random data)

Rossiter[3] derived a semi-empirical formula (Eq. 2.1), which is used to predict the acoustic mode frequencies within a low-speed open cavity flow

$$f_n = \frac{U_\infty}{L} \frac{n - \gamma}{M_\infty + \frac{1}{\kappa}} \quad (2.1)$$

where,  $f_n$  is the frequency of the given longitudinal mode and  $n$  is the longitudinal mode number,  $\gamma$  and  $\kappa$  are empirical values,  $\kappa$  is the proportion of free-stream speed at which the vortices travel over the cavity and  $\gamma$  is defined as phase lag between the time the acoustic wave reaches the leading edge and the time the vortex is shed;  $\gamma$  is a function of  $L/D$ .



# Chapter 3

## Turbulence Modeling

### 3.1 Introduction

Flow separations are of great importance especially in aeronautic applications. To predict this aerodynamic flow, classical RANS models are not capable of capturing the flow details accurately. Therefore, approaches like Detached Eddy Simulation (DES) and Large Eddy Simulation (LES) are applied to capture the flow properties more accurately. LES being more expensive numerically, DES is a reasonable choice, which is a combination of LES and RANS. One of the motivation behind development of such methods is for aeronautical applications. Among the other researchers, some initial work in this regard was carried out by Spalart et al.,(1997) [16]. The idea was to use the fine tuned RANS model in the attached boundary layer and implement LES in the separated flow region with large eddies and detached from the geometry, which cannot be captured with the traditional RANS model.

For flows with higher Reynolds number, pure LES requires a great deal of refinement near the wall regions, resulting in huge grid size. DES on the other hand uses RANS mode in the wall boundary coupled with the LES mode in the off-wall region and regions where flow is “detached“ from wall surface. RANS being computationally efficient and LES computationally more accurate, DES is a reasonably well combination to get acceptable accuracy with computational efficiency.

### 3.2 Governing Equation

The cavity flow under the present conditions is compressible. Therefore, compressible form of the continuity, momentum and energy equation are

applied. The viscous stresses and heat flux are defined by using Newton's viscosity and Fourier's heat law, respectively. The set of equation is referred to as Navier-Stokes equations.

$$\frac{\partial \rho}{\partial t} + \frac{\partial(\rho u_i)}{\partial x_i} = 0 \quad (3.1)$$

$$\frac{\partial(\rho u_i)}{\partial t} + \frac{\partial(\rho u_i u_j)}{\partial x_j} = -\frac{\partial p}{\partial x_i} + \frac{\partial \tau_{ij}}{\partial x_j} \quad (3.2)$$

$$\frac{\partial(\rho e_o)}{\partial t} + \frac{\partial(\rho e_o u_j)}{\partial x_j} = -\frac{\partial(p u_j)}{\partial x_j} + C_p \frac{\partial}{\partial x_j} \left( \left( \frac{\mu}{Pr} \right) \frac{\partial T}{\partial x_j} \right) + \frac{\partial(u_i \tau_{ij})}{\partial x_j} \quad (3.3)$$

Where  $\tau_{ij}$  in Eqns. 3.2 and 3.3 is viscous stresses. For Newtonian fluids, assuming stokes law for mono-atomic gas, the viscous stresses are given by

$$\tau_{ij} = 2\mu S_{ij}^* \quad (3.4)$$

Where,  $S_{ij}^*$  is the trace-less viscous strain rate defined by

$$S_{ij}^* \equiv \frac{1}{2} \left( \frac{\partial u_i}{\partial x_j} + \frac{\partial u_j}{\partial x_i} \right) - \frac{1}{3} \frac{\partial u_k}{\partial x_k} \delta_{ij} \quad (3.5)$$

The term  $Pr$  in Eqn. 3.3 is Laminar Prandtl number ( $Pr$ ) and is defined as

$$Pr \equiv \frac{C_p \mu}{\lambda} \quad (3.6)$$

To close these equations, it is also necessary to specify the equation of state. Furthermore, the pressures and temperatures for the present simulation are assumed to be moderate for the assumption of calorically perfect gas (i.e. internal energy and enthalpy are linear functions of temperature). Following equations are valid Eqn. 3.7.

$$\begin{aligned} p &= \rho R T \\ \gamma &\equiv \frac{C_p}{C_v} \\ e &\equiv C_v T \\ C_p - C_v &= R \end{aligned} \quad (3.7)$$

where  $R$  is the gas constant.  $C_p$  and  $C_v$  are specific heat at constant pressure and volume, respectively.

By definition the total energy ( $e_o$ ) is given by

$$e_o \equiv e + \frac{u_k u_k}{2} \quad (3.8)$$

### 3.2.1 Fluid Modeling

For fluid modeling, as discussed above, the perfect gas law is used

$$p = \rho r T \quad (3.9)$$

where  $r$  is the gas constant for perfect gas and is defined as:

$$r = \frac{R}{M} \quad (3.10)$$

Where  $R$  is universal gas constant and  $M$  is the molecular weight of the perfect gas.

#### Calorically Perfect Gas

For low temperature condition flow, where vibrational and electronic modes are not present, the internal energy of the gas is proportional to temperature. This means  $\gamma$ ,  $C_p$ ,  $C_v$  and  $R$  are constants. For moderate speed aerodynamics the assumption of calorically perfect gas stands valid and  $r$  and  $C_p$  are related as:

$$r = \frac{\gamma - 1}{\gamma} C_p \quad (3.11)$$

#### Thermally Perfect Gas

For higher temperature flows, we treat the flow as thermally perfect gas. In this case the internal energy is varied by excitation of the translational, rotational, vibrational and electronic modes of the gas molecules and no chemical reaction or ionization occur, meaning internal energy is only function of temperature. Therefore, it can be treated as thermally perfect. In this case the specific heats are now functions of Temperature. Thermally perfect gas assumption is also valid for mixing of different thermally perfect gases. For each gas and its fraction of total density, an equation is solved.

### 3.2.2 Time average Navier Stokes

For turbulence the flow quantities are decomposed into two parts the time-averaged and fluctuating quantities. In order to get the average form of the governing equation, the following time averaging methods are used.

For any dependent variable  $\phi$ ,

**Reynolds Averaging**, also known as classical time averaging, reads

$$\begin{aligned} \phi' &\equiv \phi - \bar{\phi} \\ \bar{\phi} &\equiv \frac{1}{T} \int_T \phi(t) dt \end{aligned} \quad (3.12)$$

**Favre Averaging**, is used for compressible flows, also referred as density wight time averaging. It is achieved as explained below.

$$\begin{aligned}\phi'' &\equiv \phi - \tilde{\phi} \\ \tilde{\phi} &\equiv \frac{\rho\phi}{\bar{\rho}}\end{aligned}\quad (3.13)$$

For above definitions  $\overline{\phi'} = 0$  and  $\overline{\phi''} \neq 0$

By using these averaging methods on the instantaneous continuity equation 3.1, momentum equation 3.2 and energy equation 3.3, time average form of equation is achieved. This is done by introducing density weighted time average decomposition of  $u_i$  and  $e_o$  and standard decomposition for  $\rho$  and  $p$  giving the following equations.

$$\frac{\partial \bar{\rho}}{\partial t} + \frac{\partial(\bar{\rho}\tilde{u}_i)}{\partial x_i} = 0 \quad (3.14)$$

$$\frac{\partial(\bar{\rho}\tilde{u}_i)}{\partial t} + \frac{\partial(\bar{\rho}\tilde{u}_i\tilde{u}_j)}{\partial x_j} = -\frac{\partial \bar{p}}{\partial x_i}\delta_{ij} + \frac{\partial \overline{\tau_{ij}}}{\partial x_j} - \frac{\partial}{\partial x_j}(\overline{\rho u_i'' u_j''}) \quad (3.15)$$

$$\frac{\partial(\bar{\rho}\tilde{e}_o)}{\partial t} + \frac{\partial(\bar{\rho}\tilde{u}_j\tilde{e}_o)}{\partial x_j} = -\frac{\partial}{\partial x_j}(\tilde{u}_j\bar{p} + \overline{u_j'' p}) - \frac{\partial}{\partial x_j}(\overline{\rho u_j'' e_o''}) - \frac{\partial \bar{q}_j}{\partial x_j} + \frac{\partial}{\partial x_j}(\overline{u_i \tau_{ij}}) \quad (3.16)$$

The term  $\tilde{e}_o$  is the density averaged total energy given by:

$$\tilde{e}_o \equiv \tilde{e} + \frac{\tilde{u}_k \tilde{u}_k}{2} + k \quad (3.17)$$

Where the turbulent kinetic energy  $k$  is defined by:

$$k = \frac{\widetilde{u_k'' u_k''}}{2} \quad (3.18)$$

In time average equations heat flux,  $\bar{q}_j$ , is given as:

$$\bar{q}_j = -C_p \frac{\mu}{P_r} \overline{\frac{\partial T}{\partial x_j}} \quad (3.19)$$

### 3.3 Turbulence Models

For turbulent flow calculations, different turbulence models are available. These are categorized into three main groups, namely, RANS (Reynolds-Average Navier-Stokes), DES (Detached Eddy Simulation) and hybrid RANS-LES, as well as LES (Large Eddy Simulation). These modeling approaches

can be selected in the input file by setting  $ITURB = 2$  for RANS,  $ITURB = 3$  for DES and hybrid RANS-LES and finally  $ITURB = 4$  for LES modeling. For each modeling approach, different turbulence models are available for selection. Depending upon type of flow features involved and desired analysis, the best suited turbulence model can be selected with the variable `TURB_MOD_NAME` in edge input file.

### 3.3.1 Close Form of Favre average Navier Stokes

The Eqns.3.14, 3.15 and 3.16 are referred as Favre averaged Navier Stokes equations.  $\bar{p}$ ,  $\tilde{u}_i$  and  $\tilde{e}_o$  are the primary solution variables. This group of equations contains several unknown correlation terms and is an open set of partial differential equation. To solve this set of equations some correlation terms needs to be modeled to obtain the closed form of equation.

#### Approximation and modelling

The unknown terms are rewritten as following.

$$\overline{\tau_{ij}} = \widetilde{\tau_{ij}} + \overline{\tau_{ij}''} \quad (3.20)$$

$$\overline{u_j'' p} + \overline{\rho u_j'' e_o''} = C_p \overline{\rho u_j'' T} + \tilde{u}_i \overline{\rho u_i'' u_j''} + \frac{\overline{\rho u_j'' u_i'' u_i''}}{2} \quad (3.21)$$

$$\overline{q_j} = -C_p \frac{\overline{\mu \partial T}}{P_r \partial x_j} = -C_p \frac{\mu \partial \tilde{T}}{P_r \partial x_j} - C_p \frac{\mu \partial \overline{T''}}{P_r \partial x_j} \quad (3.22)$$

$$\overline{u_i \tau_{ij}} = \tilde{u}_i \widetilde{\tau_{ij}} + \overline{u_i'' \tau_{ij}} + \tilde{u}_i \overline{\tau_{ij}''} \quad (3.23)$$

By inserting these terms in Favre averaged Navier Stokes equation gives.

$$\frac{\partial \bar{\rho}}{\partial t} + \frac{\partial(\bar{\rho} \tilde{u}_i)}{\partial x_i} = 0 \quad (3.24)$$

$$\frac{\partial(\bar{\rho} \tilde{u}_i)}{\partial t} + \frac{\partial(\bar{\rho} \tilde{u}_i \tilde{u}_j)}{\partial x_j} = -\frac{\partial}{\partial x_j} \left( \bar{p} \delta_{ij} - \widetilde{\tau_{ij}} - \underbrace{\overline{\tau_{ij}''}}_{2^*} + \underbrace{\overline{\rho u_i'' u_j''}}_{1^*} \right) \quad (3.25)$$

$$\begin{aligned}
\frac{\partial(\bar{\rho}\tilde{e}_o)}{\partial t} + \frac{\partial(\bar{\rho}\tilde{u}_j\tilde{e}_o)}{\partial x_j} = & -\frac{\partial}{\partial x_j}(\tilde{u}_j\bar{p} + \underbrace{C_p\overline{\rho u_j'' T}}_{3^*} + \underbrace{\tilde{u}_i\overline{\rho u_i'' u_j''}}_{4^*} + \underbrace{\frac{\overline{\rho u_j'' u_i'' u_i''}}{2}}_{5^*} - \\
& \underbrace{C_p\frac{\mu}{Pr}\frac{\partial\tilde{T}}{\partial x_j}}_{6^*} - \underbrace{C_p\frac{\mu}{Pr}\frac{\partial\overline{T''}}{\partial x_j}}_{6^*} - \underbrace{\tilde{u}_i\widetilde{\tau}_{ij}}_{7^*} - \underbrace{\overline{u_i''\tau_{ij}}}_{7^*} - \underbrace{\tilde{u}_i\overline{\tau_{ij}''}}_{8^*}
\end{aligned} \tag{3.26}$$

The terms highlighted from 1\*-8\* are the unknown terms, that have to be modeled in some way. Term 1\* and 4\* can be modeled using eddy-viscosity assumption of the Reynolds stresses.

$$\tau_{ij}^{turb} \equiv -\overline{\rho u_i'' u_j''} \approx 2\mu_t\widetilde{S}_{ij}^* - \frac{2}{3}\bar{\rho}k\delta_{ij} \tag{3.27}$$

where,  $\mu_t'$  is the turbulent viscosity with the last term added so that the trace is  $-2\rho k$ .

Term 2\* and 8\* are neglected since

$$|\widetilde{\tau}_{ij}| \gg |\overline{\tau_{ij}''}| \tag{3.28}$$

Term 3\*, corresponding to turbulent transport of heat can be modeled using the gradient of the turbulent heat flux.

$$q_j^{turb} \equiv C_p\overline{\rho u_j'' T} \approx -C_p\frac{\mu_t}{Pr_t}\frac{\partial\tilde{T}}{\partial x_j} \tag{3.29}$$

where  $Pr_t$  is the turbulent Prandtl number. Often a constant value of turbulent Prandtl number is used ( $Pr_t \approx 0.9$ ).

The term 5\* and 7\*, corresponding to the turbulent transport and molecular diffusion of turbulent energy respectively, can be neglected if the turbulent energy is small compared to the enthalpy.

$$k \ll \tilde{h} = C_p\tilde{T} \tag{3.30}$$

This approximation is valid for most of the flows below the hyper-sonic regime. A better approximation might be a gradient expression of form:

$$\overline{\rho u_j'' u_i'' u_i''} - \overline{u_i''\tau_{ij}} \approx -(\mu + \frac{\mu_t}{\sigma_k})\frac{\partial k}{\partial x_j} \tag{3.31}$$

where,  $\sigma_k$  is a model constant. This is not used in Eqn. 3.35 below but neglected.

Term 6\* is an artifact from Favre averaging. It is related to the heat conduction effects associated with temperature fluctuations. It can be neglected if

$$\left| \frac{\partial^2 \widetilde{T}}{\partial x_j^2} \right| \gg \left| \frac{\partial^2 \overline{T''}}{\partial x_j^2} \right| \quad (3.32)$$

This is virtually true for all the flows and hence it is neglected.

By applying all the approximations and assumptions the final closed form of the Favre averaged Navier Stokes equation is achieved as following.

$$\frac{\partial \overline{\rho}}{\partial t} + \frac{\partial (\overline{\rho \tilde{u}_i})}{\partial x_i} = 0 \quad (3.33)$$

$$\frac{\partial (\overline{\rho \tilde{u}_i})}{\partial t} + \frac{\partial (\overline{\rho \tilde{u}_i \tilde{u}_j})}{\partial x_j} = -\frac{\partial \overline{p}}{\partial x_j} \delta_{ij} + \frac{\partial \widetilde{\tau_{ij}^{Tot}}}{\partial x_j} \quad (3.34)$$

$$\frac{\partial (\overline{\rho \tilde{e}_o})}{\partial t} + \frac{\partial \overline{\rho \tilde{u}_j \tilde{e}_o}}{\partial x_j} = -\frac{\partial}{\partial x_j} \left( \tilde{u}_j \overline{p} + \widetilde{q_j^{Tot}} + \tilde{u}_i \widetilde{\tau_{ij}^{Tot}} \right) \quad (3.35)$$

where,

$$\widetilde{\tau_{ij}^{Tot}} = \widetilde{\tau_{ij}^{lam}} + \widetilde{\tau_{ij}^{turb}} \quad (3.36)$$

$$\widetilde{\tau_{ij}^{lam}} \equiv \widetilde{\tau_{ij}} = \mu \left( \frac{\partial \tilde{u}_i}{\partial x_j} + \frac{\partial \tilde{u}_j}{\partial x_i} - \frac{2}{3} \frac{\partial \tilde{u}_k}{\partial x_k} \delta_{ij} \right) \quad (3.37)$$

$$\widetilde{\tau_{ij}^{turb}} \equiv -\overline{\rho u_i'' u_j''} \approx \mu_t \left( \frac{\partial \tilde{u}_i}{\partial x_j} + \frac{\partial \tilde{u}_j}{\partial x_i} - \frac{2}{3} \frac{\partial \tilde{u}_k}{\partial x_k} \delta_{ij} \right) - \frac{2}{3} \overline{\rho} k \delta_{ij} \quad (3.38)$$

$$\widetilde{q_j^{Tot}} \equiv \widetilde{q_j^{lam}} + \widetilde{q_j^{turb}} \quad (3.39)$$

$$\widetilde{q_j^{lam}} \equiv \tilde{q}_j \approx -C_p \frac{\mu}{Pr} \frac{\partial \widetilde{T}}{\partial x_j} = \frac{\gamma}{\gamma - 1} \frac{\mu}{Pr} \frac{\partial}{\partial x_j} \left( \frac{\overline{p}}{\overline{\rho}} \right) \quad (3.40)$$

$$\widetilde{q_j^{turb}} \equiv C_p \overline{\rho u_j'' T} \approx -C_p \frac{\mu_t}{Pr_t} \frac{\partial \widetilde{T}}{\partial x_j} = \frac{\gamma}{\gamma - 1} \frac{\mu_t}{Pr_t} \frac{\partial}{\partial x_j} \left( \frac{\overline{p}}{\overline{\rho}} \right) \quad (3.41)$$

$$\overline{p} = (\gamma - 1) \overline{\rho} \left( \tilde{e}_o - \frac{\tilde{u}_k \tilde{u}_k}{2} - k \right) \quad (3.42)$$

If a separate turbulence model is used to solve for  $\mu_t$ ,  $k$  and  $Pr_t$ , and gas data is given for  $\mu$ ,  $\gamma$  and  $Pr$  than these equations form a closed set of partial differential equation which can be solved numerically.

### 3.3.2 Spalart Allmaras One-equation model

The model solves one transport equation for a quantity of “ $\tilde{\nu}$ ” (kinematic eddy viscosity parameter). The turbulence is characterized by the length scales and the velocity scales, see ref: Spalart et al.,(1994)[17]. The model only solves for one property, additional information is needed. In one-equation model the length scale cannot be computed, but must be specified to determine the rate of dissipation of the transported turbulence quantity. the model is integrated all the way to the wall which requires a good resolution of mesh normal to the wall surface ( $y^+ \sim 1$ ). The (dynamic) eddy viscosity is related to  $\tilde{\nu}$  by

$$\begin{aligned}\mu_t &= \rho \tilde{\nu} f_{\nu 1} \\ f_{\nu 1} &= \frac{\chi^3}{\chi^3 + C_{\nu 1}^3} \\ \chi &\cong \frac{\tilde{\nu}}{\nu}\end{aligned}\tag{3.43}$$

$f_{\nu 1} = f_{\nu 1} \left( \frac{\tilde{\nu}}{\nu} \right)$ , which tends to unity for higher Reynolds numbers.  
 $\Rightarrow \tilde{\nu} = \nu_t$  and at wall  $f_{\nu 1} \rightarrow 0$

The Reynolds stresses are computed with

$$\tau_{ij} = -\overline{\rho u'_i u'_j} = 2\mu_t S_{ij} = \rho \tilde{\nu} f_{\nu 1} \left( \frac{\partial \overline{u_i}}{\partial x_j} + \frac{\partial \overline{u_j}}{\partial x_i} \right)\tag{3.44}$$

The transport equation for  $\tilde{\nu}$  is as following:

$$\begin{aligned}\frac{\partial(\rho \tilde{\nu})}{\partial t} + \frac{\partial(\rho \tilde{\nu} \overline{u_i})}{\partial x_i} &= \frac{1}{\sigma_\nu} \left( \frac{\partial}{\partial x_i} \left( (\mu + \rho \tilde{\nu}) \frac{\partial \tilde{\nu}}{\partial x_i} \right) + C_{b2} \rho \frac{\partial \tilde{\nu}}{\partial x_j} \frac{\partial \tilde{\nu}}{\partial x_j} \right) \\ &+ C_{b1} \rho \tilde{\nu} \tilde{\Omega} - C_{w1} \rho \left( \frac{\tilde{\nu}}{d} \right)^2 f_w\end{aligned}\tag{3.45}$$

where,

$$\tilde{\Omega} = \Omega + \frac{\tilde{\nu}}{(\kappa y)^2} f_{\nu 2}\tag{3.46}$$

$$\begin{aligned}\Omega &= \sqrt{2\Omega_{ij}\Omega_{ij}} = \text{mean vorticity} \\ \Omega_{ij} &= \frac{1}{2} \left( \frac{\partial \overline{u_i}}{\partial x_j} + \frac{\partial \overline{u_j}}{\partial x_i} \right) = \text{mean vorticity tensor} \\ d &= \kappa y \\ f_{\nu 2} &= f_{\nu 2} \left( \frac{\tilde{\nu}}{\nu} \right) \\ f_w &= f_w \left( \frac{\tilde{\nu}}{\Omega \kappa^2 y^2} \right)\end{aligned}\tag{3.47}$$

$f_{\nu 2}$  and  $f_w$  are the wall damping functions. Inspection of destruction term reveal that  $\kappa y$  (with  $y =$  distance to the wall) has been used as length scale.

The length scale  $\kappa y$  also enters in the vorticity parameter  $\Omega$  and is just equal to the mixing layer length.

The model constants are as following:

$$\begin{aligned}
\sigma_n u &= \frac{2}{3} \\
\kappa &= 0.4187 \\
C_{b1} &= 0.1355 \\
C_{b2} &= 0.622 \\
C_{w1} &= C_{b1} + \kappa^2 \frac{1+C_{b2}}{\sigma_\nu}
\end{aligned} \tag{3.48}$$

### 3.3.3 Wilcox Standard $k - \omega$ turbulence model

The Wilcox standard  $k - \omega$  model [18](written in conservation form) is given by the following:

For turbulent kinetic energy  $k$ ,

$$\frac{\partial(\rho k)}{\partial t} + \frac{\partial(\rho u_j k)}{\partial x_j} = P - \beta^* \rho \omega k + \frac{\partial}{\partial x_j} \left[ \left( \mu + \sigma_k \frac{\rho k}{\omega} \right) \frac{\partial k}{\partial x_j} \right] \tag{3.49}$$

For specific dissipation rate of  $k$  the following equation is used.

$$\frac{\partial(\rho \omega)}{\partial t} + \frac{\partial(\rho u_j \omega)}{\partial x_j} = \frac{\gamma \omega}{k} P - \beta \rho \omega^2 + \frac{\partial}{\partial x_j} \left[ \left( \mu + \sigma_\omega \frac{\rho k}{\omega} \right) \frac{\partial \omega}{\partial x_j} \right] \tag{3.50}$$

and the turbulent eddy viscosity is computed from

$$\mu_t = \frac{\rho k}{\omega} \tag{3.51}$$

The constants and the auxiliary functions are:

$$\begin{aligned}
\sigma_k &= 0.5 \\
\sigma_\omega &= 0.5 \\
\beta_* &= 0.09 \\
\gamma &= \frac{5}{9} \\
\beta &= \frac{3}{40}
\end{aligned} \tag{3.52}$$

One major limitation of Wilcox  $k - \omega$  model is its dependency on free-stream quantities. Near the wall the model returns low peak of turbulent kinetic energy resulting in over-prediction of specific dissipation rate. As a result the near-wall eddy viscosity is under estimated. This might result in unphysical flow solution.

$$\omega = \frac{\alpha^* \varepsilon}{c_\mu k} \tag{3.53}$$

### 3.3.4 SST Menter $k - \omega$ turbulence model

The SST Menter  $k - \omega$  model [19] is developed to resolve the free stream dependency problem resulting in unphysical flow solution. To achieve this a cross diffusion term is added to the  $k - \omega$  model. The model uses  $k - \varepsilon$  formulation in the outer part of the boundary layer and uses the Wilcox  $k - \omega$  model near the wall part of the boundary layer. The transformation from  $k - \varepsilon$  to  $k - \omega$  is achieved by introduction of cross diffusion term and modified coefficients which are implemented by a blending function.

The closed form of the SST Menter  $k - \omega$  model is as following.

For turbulent kinetic energy  $k$ ,

$$\frac{\partial(\rho k)}{\partial t} + \frac{\partial(\rho u_j k)}{\partial x_j} = P - \beta^* \rho \omega k + \frac{\partial}{\partial x_j} \left[ (\mu + \sigma_k \mu_t) \frac{\partial k}{\partial x_j} \right] \quad (3.54)$$

For specific dissipation rate of  $k$ ,

$$\begin{aligned} \frac{\partial(\rho \omega)}{\partial t} + \frac{\partial(\rho u_j \omega)}{\partial x_j} = \frac{\gamma}{\nu_t} P - \beta \rho \omega^2 + \frac{\partial}{\partial x_j} \left[ (\mu + \sigma_\omega \mu_t) \frac{\partial \omega}{\partial x_j} \right] + \\ 2(1 - F_1) \frac{\rho \sigma_{\omega 2}}{\omega} \frac{\partial k}{\partial x_j} \frac{\partial \omega}{\partial x_j} \end{aligned} \quad (3.55)$$

Where kinematic eddy viscosity is given as

$$\mu_t = \frac{\rho a_1 k}{\max(a_1 \omega, \Omega F_2)} \quad (3.56)$$

and

$$\begin{aligned} P &= \tau_{ij} \frac{\partial u_i}{\partial x_j} \\ \tau_{ij} &= \mu_t \left( 2S_{ij} - \frac{2}{3} \frac{\partial u_k}{\partial x_k} \delta_{ij} \right) - \frac{2}{3} \rho k \delta_{ij} \\ S_{ij} &= \frac{1}{2} \left( \frac{\partial u_i}{\partial x_j} + \frac{\partial u_j}{\partial x_i} \right) \end{aligned} \quad (3.57)$$

Each constant is a mix of inner and outer constant blended by the function

$$\phi = F_1 \phi_1 + (1 - F_1) \phi_2 \quad (3.58)$$

where,  $\phi_1$  and  $\phi_2$  represents the inner and outer constants respectively. Additional relations are

$$\begin{aligned}
\phi &= F_1\phi_1 + (1 - F_1)\phi_2 \\
F_1 &= \tanh(\arg_1^4) \\
\arg_1 &= \min \left[ \max \left( \frac{\sqrt{k}}{\beta^*\omega d}, \frac{500\nu}{d^2\omega} \right), \frac{4\rho\sigma_{\omega 2}k}{CD_{k\omega}d^2} \right] \\
CD_{k\omega} &= \max \left( 2\rho\sigma_{\omega 2} \frac{1}{\omega} \frac{\partial k}{\partial x_j} \frac{\partial \omega}{\partial x_j}, 10^{-20} \right) \\
F_2 &= \tanh(\arg_2^2) \\
\arg_2 &= \max \left( 2 \frac{\sqrt{k}}{\beta^*\omega d}, \frac{500\nu}{d^2\omega} \right)
\end{aligned} \tag{3.59}$$

and  $\rho$  is the density,  $\nu_t = \mu_t/\rho$  is the turbulent kinetic viscosity,  $\mu$  is the molecular dynamic viscosity,  $d$  is the distance from the field point to the nearest wall, and  $\Omega$  is the vorticity magnitude. The model constants are as following.

$$\begin{aligned}
\alpha_1 &= \frac{5}{9} \\
\alpha_2 &= 0.44 \\
\beta_1 &= \frac{3}{40} \\
\beta_2 &= 0.0828 \\
\beta^* &= \frac{9}{100} \\
\sigma_{k1} &= 0.85 \\
\sigma_{k2} &= 1 \\
\sigma_{\omega 1} &= 0.5 \\
\sigma_{\omega 2} &= 0.856
\end{aligned} \tag{3.60}$$

### 3.3.5 Explicit Algebraic Reynolds Stress Models (EARSM)

In the industrial flow computations standard two-equation models are still dominant. Flows associated with strong streamline curvatures, flow separation and adverse pressure gradient are not accurately predicted by these models. In the EARSM by Willin et al.,(2000)[20] improvements are made to the standard two-equation models in order to compute the complex turbulent flows more accurately (Willin et al.,(2002)[21]). Transport equations for the individual Reynolds stress anisotropies are introduced (replacing the boussinesq hypothesis) since these sets of equations deals well with the associated complex dynamics of inter-component transfer. The Reynolds stress anisotropy may be considered constant in time and space. The Reynolds stress tensor is explicitly expressed in terms of the velocity gradient and the turbulence scales.

The Explicit Algebraic Reynolds Stress Model(EARSM) consists an anisotropy tensor  $a$  which can be expressed in terms of strain- and rotation rate tensors  $S$  and  $\Omega$  as

$$a = \sum_{\lambda=1}^1 \beta_{\lambda} T^{(\lambda)} \quad (3.61)$$

where, the  $\beta$  coefficients are computed using the five invariants of  $S$  and  $\Omega$ . The  $T$ 's are as followings

$$\begin{aligned} T^{(1)} &= S, \\ T^{(2)} &= S^2 - \frac{1}{3} I I_s I, \\ T^{(3)} &= \Omega^2 - \frac{1}{3} I I_{\Omega} I, \\ T^{(4)} &= S\Omega - \Omega S, \\ T^{(5)} &= S^2\Omega - \Omega S^2, \\ T^{(6)} &= S\Omega^2 + \Omega^2 S - \frac{2}{3} I V I, \\ T^{(7)} &= S^2\Omega^2 + \Omega^2 S^2 - \frac{2}{3} V I, \\ T^{(8)} &= S\Omega S^2 - S^2\Omega S^2, \\ T^{(9)} &= \Omega S\Omega^2 - \Omega^2 S\Omega, \\ T^{(10)} &= \Omega S^2\Omega^2 - \Omega^2 S^2\Omega. \end{aligned} \quad (3.62)$$

The Reynolds stress tensors is then related to the anisotropy as

$$\overline{\rho u_i u_j} = \rho k \left( a_{ij} + \frac{2}{3} \delta_{ij} \right) \quad (3.63)$$

In this model the turbulent stress relation is given by:

$$\tau_{ij} = 2\mu_t \left( S_{ij} - \frac{2}{3} \rho k \delta_{ij} - a_{ij}^{ex} \rho k \right) \quad (3.64)$$

The Conservative form of the two-equation model is given as  
For turbulent kinetic energy  $k$ ,

$$\frac{\partial(\rho k)}{\partial t} + \frac{\partial(\rho u_j k)}{\partial x_j} = P - \beta^* \rho \omega k + \frac{\partial}{\partial x_j} \left[ (\mu + \sigma_k \mu_t) \frac{\partial k}{\partial x_j} \right] \quad (3.65)$$

For specific dissipation rate of  $k$ ,

$$\begin{aligned} \frac{\partial(\rho \omega)}{\partial t} + \frac{\partial(\rho u_j \omega)}{\partial x_j} &= \frac{\gamma \omega}{k} P - \beta \rho \omega^2 + \frac{\partial}{\partial x_j} \left[ (\mu + \sigma_{\omega} \mu_t) \frac{\partial \omega}{\partial x_j} \right] \\ &+ \sigma_d \frac{\rho}{\omega} \max \left( \frac{\partial k}{\partial x_k} \frac{\partial \omega}{\partial x_k}, 0 \right) \end{aligned} \quad (3.66)$$

where  $\rho$  is the density and  $\mu$  is the molecular dynamic viscosity, and

$$\begin{aligned}
P &= \tau_{ij} \frac{\partial u_i}{\partial x_j} \\
S_{ij} &= \frac{1}{2} \left( \frac{\partial u_i}{\partial x_j} + \frac{\partial u_j}{\partial x_i} \right) \\
S_{ij}^* &= \frac{\tau}{2} \left( \frac{\partial u_i}{\partial x_j} + \frac{\partial u_j}{\partial x_i} \right) \\
W_{ij}^* &= \frac{\tau}{2} \left( \frac{\partial u_i}{\partial x_j} - \frac{\partial u_j}{\partial x_i} \right) \\
\tau &= \frac{1}{\beta^* \omega}
\end{aligned} \tag{3.67}$$

and the turbulent eddy viscosity is calculated as

$$\mu_t = \frac{C_\mu \rho k}{\beta^* \omega} \tag{3.68}$$

where

$$C_\mu = -\frac{1}{2} (\beta_1 + II_\omega \beta_6) \tag{3.69}$$

Furthermore,

$$\begin{aligned}
\beta_1 &= -\frac{N(2N^2 - 7II_\Omega)}{Q} \\
\beta_3 &= -\frac{12(IV)}{NQ} \\
\beta_4 &= -\frac{2(N^2 - 2II_\Omega)}{Q} \\
\beta_6 &= -\frac{6N}{Q} \\
\beta_9 &= \frac{6}{Q} \\
Q &= \frac{5}{6}(N^2 - 2II_\Omega)(2N^2 - II_\Omega) \\
II_\Omega &= W_{kl}^* W_{kl}^* \\
IV_\Omega &= S_{kl}^* W_{lm}^* W_{mk}^*
\end{aligned} \tag{3.70}$$

and  $N$  is obtained from the solution of a cubic equation. For more details about the model, read Willin et al.,(2000)[20] and Hellsten .,(2005) [22]. In case of geometries associated with strong curvatures resulting in high rotation the EARSM approximation is not perfectly valid. However, Willin et al.,(2002) [21] provided an approximation of the missing terms in the model.

$$W_{ij}^* = \frac{\tau}{2} \left( \frac{\partial u_i}{\partial x_j} - \frac{\partial u_j}{\partial x_i} \right) - \left( \frac{\tau}{A_o} \right) W_{ij}^{*(r)} \tag{3.71}$$

where

$$\begin{aligned}
W_{ij}^{*(r)} &= -\varepsilon_{ijk} B_{km} S_{pr}^* \frac{DS_{r,q}^*}{Dt} \varepsilon_{pqm} \\
B_{km} &= \frac{II_S^2 \delta_{km} + 12III_S S_{km}^* + 6II_S S_{kl}^* S_{lm}^*}{2II_S^3 - 12III_S^2}
\end{aligned} \tag{3.72}$$

and  $A_o = -0.72$ ,  $III_S = S_{kl}^* S_{lm}^* S_{mk}^*$  and  $\varepsilon_{ijk}$  is the Levi-Civita symbol, defined as

$$\begin{aligned}\varepsilon_{123} &= \varepsilon_{312} = \varepsilon_{231} = 1 \\ \varepsilon_{132} &= \varepsilon_{213} = \varepsilon_{321} = -1\end{aligned}\tag{3.73}$$

with all other  $\varepsilon_{ijk} = 0$ . Further information can be found in the references, Wallin et al.,(2002) [21] and Hellsten .,(2005) [22].

### 3.4 Spalart-Allmaras DES Model

During the initial study of DES modeling approach, in 1997 Spalart Allmaras introduced SA-DES, Spalart et al.,(1997)[16]. This approach implemented the Spalart-Allmaras (SA) one equation model in the wall boundary region in addition to Sub-Grid-Scale (SGS) modeling approach used in LES region away from the wall. This is achieved by using the same turbulence transport equation for entire domain and switching between RANS and LES by switching the turbulent length scale.

The SA-model solves a transport equation for a working eddy viscosity,  $\tilde{\nu}$ . For further details about SA-RANS ref: Spalart et al.,(1994) [17] and for SA-DES ref: Spalart et al.,(1997) [16]. The SA-turbulence model contains a destruction term for its eddy viscosity  $\tilde{\nu}$ , which is proportional to  $(\tilde{\nu}/d)^2$ , where 'd' is the distance to the closest wall. The destruction term when balance with the production term, adjusts the eddy viscosity to scale with the local deformation rate 'S' and 'd':  $\tilde{\nu} \propto Sd^2$ . the smagorinsky model scales SGS eddy viscosity with S and the grid size  $\Delta$ :  $\nu_{sgs} \propto S\Delta^2$ .

In DES formulation ' $\tilde{d}$ ' is introduced, when the turbulent length scale ' $\tilde{d}$ ' is taken equal to wall distance 'd', the model behaves as original SA-RANS model. The SGS model for region away from wall is achieved by switching the turbulent length scale from wall distance to a SGS turbulent length scale in association to the local cell size. This is done by expressing:

$$\tilde{d} = \min(d, C_{des}\Delta)\tag{3.74}$$

Where,  $\Delta$  is the grid size and  $C_{des}$  is the model constant.  $C_{des}$  is calibrated in LES for decaying homogeneous isotropic turbulence (DHIT), which has a constant rate of  $C_{des} = 0.65$ . In many regions, specially in boundary layer region, highly anisotropic grids are used. We define  $\Delta$  as the largest of all spacings in all directions ( $\Delta \equiv \max(\Delta_x, \Delta_y, \Delta_z)$ ). Although typically  $\Delta_y \ll d$  and the ratio between  $(\Delta_x \Delta_y \Delta_z)^{1/3}$  and  $d$  us unclear, we do have  $d \ll \Delta$ , giving RANS behavior. If grid is finer in one direction that has no influence.

# Chapter 4

## Simulation Methods

The closed form of Navier-Stokes equation can be solved numerically for ' $u_i$ ' and ' $e_o$ '. There are variety of computational software available which can be used to solve Navier-Stokes equation. For the present case EDGE, a CFD (Computational Fluid Dynamics) flow solver for  $2D/3D$  problems with unstructured grid was used. EDGE is capable of solving viscous/inviscid, compressible problems for both steady state and unsteady time accurate calculations in parallel processing environment. For further details about EDGE read 'Edge User Guide' [23] and 'Edge Theoretical Formulation' document[24].

### 4.1 The Unstructured CFD Solver Edge

EDGE is capable of solving RANS (Reynolds Averaged Navier-Stokes) for compressible flow in rotating as well as stationary frame of references, moreover, LES (Large Eddy Simulation) and DES (Detached Eddy Simulation) could be implemented. The governing equation is solved by using node-centered finite-volume technique. The control volumes are non-overlapping and are obtained from the control surfaces of each edge in the provided mesh.

Explicit integration of the governing equation towards the steady state is achieved with Runge-kutta time integration. By using multigrid levels collectively (and cycling through them) and implicit residual smoothing, the convergence rate can be improved. The same convergence acceleration technique is used for a steady state inner iterations in time accurate computations, which are performed using semi-implicit, dual time-stepping scheme. Furthermore, EDGE includes other options like, discretization scheme, for mean flow as well as turbulence, different gas models, low speed preconditioning. EDGE also incorporates applications for Shape Optimization and Aeroelasticity.

### 4.1.1 Geometrical Considerations

For finite-volume technique the required control-volumes with the unknowns in the nodes located in center, are provided by preprocessor. This is then used as an input to the flow solver for computations. The grid with its dual grid provided by preprocessor for a 2D case is depicted in the Fig. 4.1 dual-grid below.

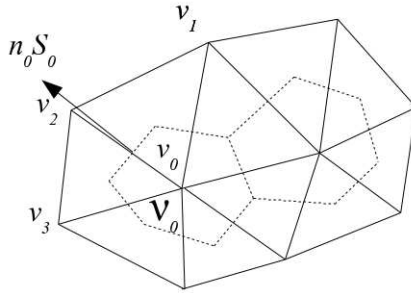


Figure 4.1: The input grid (solid) also denoted triangular grid its dual grid (dashed) forming the control volume.

The coordinates in the the input Grid provides the coordinates for each node and the connectivity between two nodes by an edge. A control surface  $nS$  is also provided for each edge where  $n$  is the normalized normal vector and  $S$  is the area. These control surfaces for respective edges, that emerge from a node enclose the control volume of that particular node. The surface normal vector  $n$  for a control volume points outwards normal to the surface of control volume. For a closed control volume the sum of surface vectors is a null vector. This check is performed for all the control volumes.

$$\sum_i n_i S_i = 0 \quad (4.1)$$

The control surface to the interior nodes is provided by all edges connected to it, forming a control volume for the respective node, whereas, apart from control surfaces provided by edges the boundary node requires a control surface separately to close it. This can be seen in Fig.4.2 with  $\nu_1$  the boundary node and  $\nu_3$  the interior.

At the corner point where two or more boundaries meet, the control surface is split into respective numbers of control surfaces, such as the boundary conditions can be applied for each boundary. This results in possibility of having one node in several boundary conditions. The boundary nodes are also supplied with an inner point at all boundaries, which are used in some

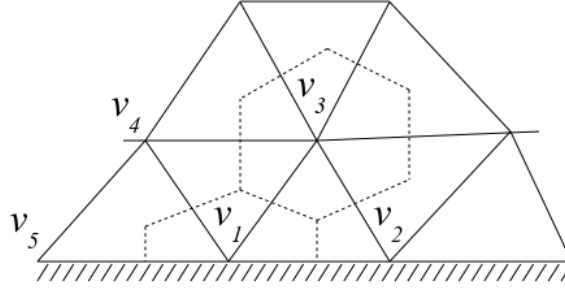


Figure 4.2: Control volumes at the inner and the boundary node.

boundary conditions. The inner node is chosen as an end node of the adjacent edge closest to boundary surface.

For 3D cases similar discretization is done. In this case the dual mesh consists of the triangular facets between the centroids of cells, the faces and the edge. The control volume of a node consists of the faces intersecting the mid-point of the edge. At the boundaries additional control faces are added to form the control volume.

## 4.2 Boundary Condition

There are two ways to implement the boundary conditions, weak/neumann and strong/dirichlet boundary conditions. Mostly the boundary conditions are specified as weak boundary conditions, which are imposed by specifying the normal derivative of the function on a surface. All the boundary nodes are updated as any interior unknown ensuring the imposed fluxes are maintained.

$$\frac{\partial T}{\partial n} = \hat{n} \cdot \nabla T = f(r, t) \quad (4.2)$$

At some boundaries a strong boundary condition is applied in which the boundary nodes are assigned a constant value which does not change through out the simulation.

$$T = f(r, t) \quad (4.3)$$

One common example of strong boundary condition is the wall boundary condition where no-slip condition is imposed by setting the wall velocity equal to zero. The boundary conditions applied in the present simulation are described below.

### 4.2.1 Wall Boundary Condition

At wall, there are three types of boundary conditions that can be specified in Edge. Euler condition, Adiabatic and Isothermal, which are chosen depending upon the case. For inviscid flows Euler wall conditions is used, which is a weak condition, since all the variables are unknown and condition is applied by specifying fluxes, at Euler wall

$$u_1 \cdot n = 0 \quad (4.4)$$

Hence wall fluxes become

$$f(n) = \begin{pmatrix} 0 \\ p_1 n_x S \\ p_1 n_y S \\ p_1 n_z S \\ 0 \end{pmatrix}$$

Similar boundary conditions are used for symmetry conditions.

For viscous flows, adiabatic and isothermal boundary conditions are used. The viscous boundary condition use strong condition on the velocity by setting it to zero, implying no-slip condition. The strong boundary condition on velocity gives better convergence and is sufficiently accurate for fine meshes, as for the weak boundary condition [25].

In case of isothermal wall a weak condition is implied on the constant wall temperature.

For viscous flow most of the boundary conditions used are weak adiabatic, which was also the choice for present simulation. This implies no-slip condition on velocity. At an adiabatic wall there is no contribution from the viscous terms to the energy equation at a wall since temperature gradients is zero.

$$\frac{\partial T}{\partial n_1} = 0 \quad (4.5)$$

This means that the boundary flux is zero for both density and energy equation. In addition to the velocity, the turbulent quantities are also imposed strongly by setting

$$\tilde{v} = 0 (\text{recommended by SA, 1992}) \quad (4.6)$$

By default it is assumed that the grid at the wall is well resolved to achieve  $y^+ \simeq 1$  in first layer of node away from the wall unless it is specified to use the wall functions. If it is specified to use the wall function, a larger value

of  $y^+$  can be used such that  $y^+ > 30$  and first inner nodes are in log-layer, where a finite velocity is specified strongly. In the present case the mesh at wall is well resolved and first layer is such that  $y^+ \simeq 1$ .

### 4.2.2 Symmetry Condition

In Edge the symmetry boundary condition are the same as in Euler condition, i.e. zero normal velocity as shown in equation 4.4.

### 4.2.3 Farfield (Weak Characteristic)

In external aerodynamic flows the external boundaries are defined as Farfield, which can handle subsonic and supersonic conditions at inflow and outflow boundaries. In farfield boundary conditions, characteristics are either set from free stream quantities for ingoing characteristics or extrapolated from free stream quantities for outgoing characteristics. This depends on the sign of the eigenvalues.

## 4.3 Running a Computation With Edge

### 4.3.1 Edge Files

To run a simulation with Edge an input file (**\*.ainp-file**) was prepared for the SA-DES computation with the freestream settings for Mach number 0.85. Preprocessor was run by providing the input file and **\*.bedg-file** was obtained. The boundary conditions were specified by running **bound** command and selecting the boundary conditions by feeding the respective number available for each specific condition. Different versions of Edge were available and it was noticed that each version have a specific format for input file and also new boundary conditions file (**\*.aboc-file**) needs to be created. Depending upon the size of the computational mesh, multi-processors can be specified to reduce the simulation time. After the simulations are done the output files are merged together by command **mergepartitions** to obtain one single **\*.bout-file**. For postprocessing the output file was transformed to a format readable by Ensign by using **ffa2engold** command. Edge also provides a list of optional post-processing variables, which were not used in present simulation. On the other hand the option to record the time-series for unsteady computations was activated. Twenty points were specified by providing their coordinates and specifying if they are on boundary or interior in the input file.

### 4.3.2 Grid

The present case is based on an experimental measurement by QinetiQ for an open rectangular cavity [26]. Mesh was provided by FOI, (Swedish Defense Research Agency), consisting of 6.18 million nodes. The mesh used is similar to the one used by FOI, for comparison of SA-DES and HYB0 model [27]. Fig. 4.3 shows the computational grid and the sketch of the geometry under consideration. The geometry is a mock-up of the experimental setup (Stanek et al., 2000), consisting of a flat plate with a cavity held in a windtunnel section with a sting. The mesh distribution can be seen in 4.3.

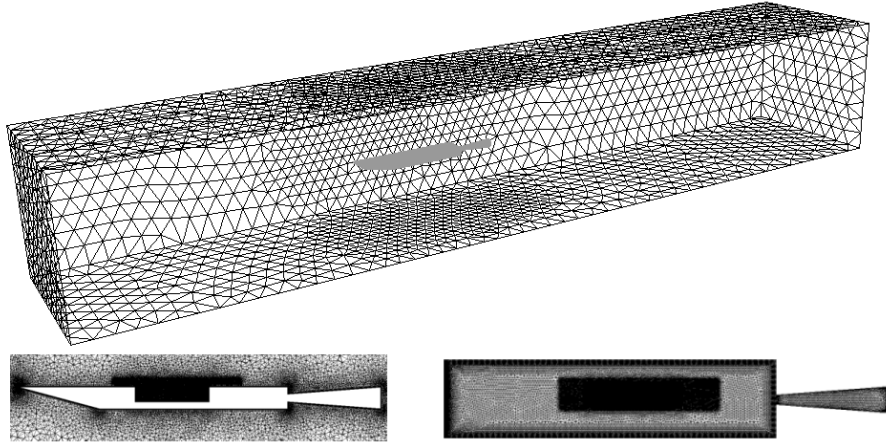


Figure 4.3: Mesh distribution over the entire domain and inside cavity

### 4.3.3 Edge Parameters

The simulation parameters are specified in the input file. Apart from few settings, most of the default values were used for the present simulation. The CFL number was also specified and tuned up to get a stable solution and accelerate convergence. Higher  $CFL$  accelerates the speed of convergence which is desirable unless instability issues arise. Multigrid option was also used in Edge to improve the time for convergence for the simulation. In case of facing numerical issues these multigrid levels can be reduced for stable solution.

### 4.3.4 Numerical Scheme

Two main discretization schemes are available in Edge. Selection can be made based on the type of flow in hand. The selection of Central differenc-

ing scheme over upwind scheme for momentum equation resides in the fact of upwind scheme being numerically more dissipative thus might result in smearing up the results and unable to capture interesting flow structures.

### 4.3.5 Boundary conditions

Correct boundary conditions play an important role in getting the correct flow. Variety of boundary conditions are available and selection is made such that the real time conditions are mimiced. At the inlet and outlet pressure far field boundary conditions are specified. Wall boundary condition was specified for the cavity walls. For the test section wall symmetry boundary condition is used.

### 4.3.6 Time Integration

The flow at hand is inherently unsteady therefore, time dependent solution is computed by also carrying out discretization in time. Several temporal discretization schemes are available. Time-step size and number of inner iterations are important parameters to achieve reasonable accuracy in each time-step and capture the transient flow details.

## 4.4 The Computational Set-up

The geometric configuration of the cavity used in this project is the mock-up of the experiment conducted by the QinetiQ [26]. Experiment was conducted by mounting the flat plate containing a rectangular cavity inside a  $8' \times 8'$  transonic wind tunnel. The plate had a length and with of 72 inches and 17 inches respectively. The rectangular cavity has dimensions of length  $L = 20$  inches, depth  $D = 4$  inches and width  $W = 4$  inches, thus resulting with aspect ratio of  $L : D : W = 5 : 1 : 1$ , see Fig.4.4. The experiment was performed under the free stream conditions of  $M_\infty = 0.85$ ,  $P_\infty = 6.21 \times 10^4 Pa$ ,  $T_\infty = 266.53$  and  $Re = 13.47 \times 10^6$  per meter.

The computational domain show in Fig. 4.4 consists of a flat plate with length  $L_x = 18D$  and width  $L_y = 7.5D$ . At the inlet and outlet Farfield boundary condition (*number31*) was specified. The freestream values at the boundary can be specified here also, if not specified the values from input files are used by default. For wind tunnel test section walls symmetry boundary condition (*number21*) was specified whereas, for cavity and mounting boundaries Adiabatic wall boundary condition (*number12*) was specified.

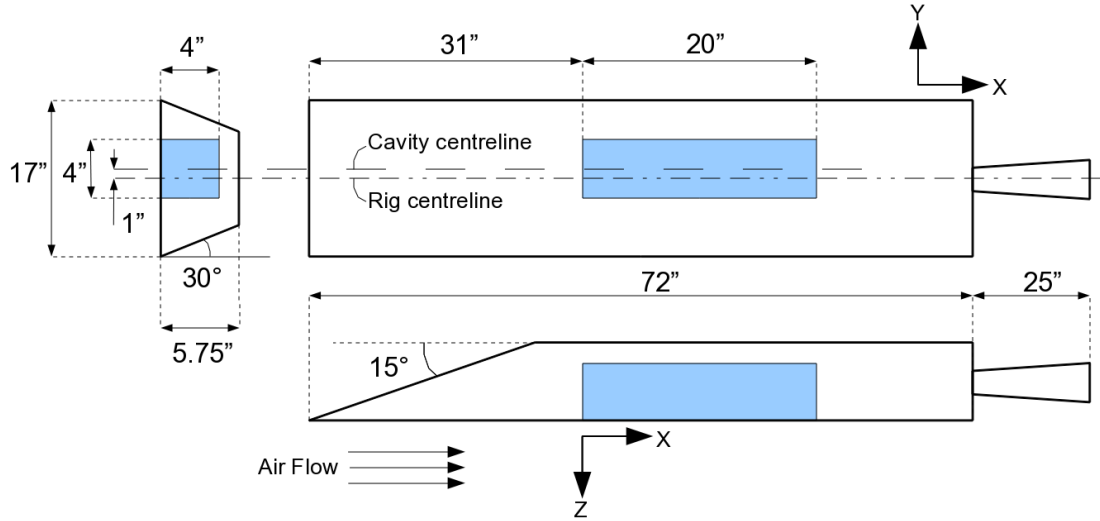


Figure 4.4: The Sketch of the cavity geometry embedded in a plate with Length and width of 72 inches and 17 inches respectively.

Here you can specify wall functions but in this case it wall functions were not used. The size of the computation demanded use of multi-processors therefore, it was specified in input file by setting **NPART** to 48. The *CFL* number was set to 1.25 in the beginning and than later on increased to 1.75 since there were no issues with the instability in the simulation. Four levels of multigrid were selected with a default settings of *W - cycle*. The Spalart-Allmaras model is selected in Edge by setting *ITURB* = 3, and *TURB\_MOD\_NAME* = 'Spalart - AllmarasDESmodel'. For the DES the central difference scheme was used with second order implicit time integration. Central Differencing scheme was also used for the turbulent transport equations. Pressure far field conditions were applied on the inflow and outflow boundaries with freestream conditions of Mach number  $M = 0.85$ , temperature  $T = 266.528 K$ , pressure  $P = 62096 Pa$  and eddy viscosity ratio of  $\mu_t/\mu_0 = 10$ . The five cavity walls and the geometry walls containing the cavity are specified as adiabatic wall boundary with no-slip condition. The ideal boundary condition for the outer (wind tunnel section) walls would have been non-reflective boundary condition. Whereas, the best available boundary condition was symmetry which was applied. The DES computation was initialized with the Reynolds-averaged Navier-Stokes (RANS) solution. A time-step size of  $2 \times 10^{-5}$  seconds was selected on the basis of study made by Larcheveque et al. (2001) [4] suggesting that a time-step around  $\Delta t = 2 \times 10^{-5}$  or smaller should be sufficient for this particular test case. A maximum of 70 inner iterations were carried out for

each time-step to ensure adequate convergence. The computations were run for a total of 13,000 time-steps or 0.26 seconds real time. The time averaging was started after first 2000 iterations, ensuring the flow is developed inside the cavity.



# Chapter 5

## Results and Discussion

### 5.1 2D Results

The study of the flow over a cavity was started with 2D computations to understand the basic flow physics and compare the effect of different turbulence models. The turbulence models used for the computations include the SA, EARSM, SST k- $\omega$  and Wilcox turbulence models.

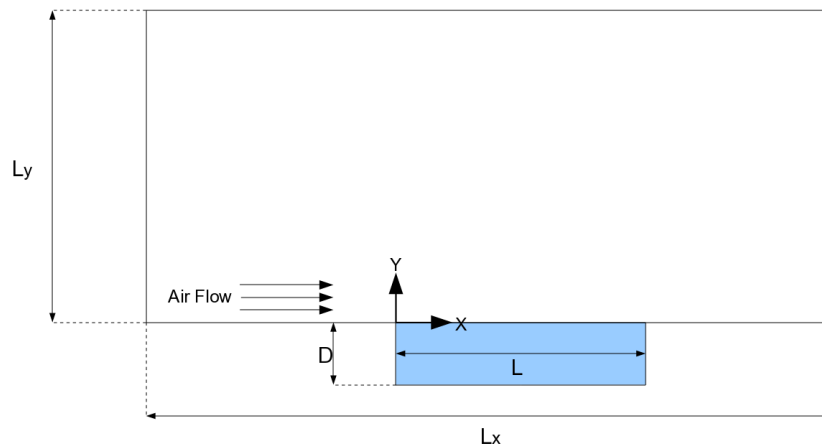


Figure 5.1: Computational domain used for 2D simulations

#### 5.1.1 Computational setup

The computational domain used for carrying out 2D simulations is shown in Fig. 5.1. The domain size in x-direction and y-direction are  $L_x = 18D$  and  $L_y = 7.5D$  respectively. The leading edge of the cavity is located at a

distance of  $7.65D$  from the flow inlet whereas, the outlet of the domain is downstreams at a distance of  $5.25D$  from the trailing edge of the cavity. On the wall surfaces, adiabatic wall boundary candidates are applied. At the top surface of the domain (at  $y = L_y$ ) symmetry boundary conditions are used. The inlet and outlet boundary conditions are specified as the external boundary conditions, which is weak characteristic boundary condition. The mesh used consists of 51410 nodes with  $176 \times 96$  nodes inside the cavity and  $352 \times 96$  nodes above the cavity. The computational mesh used for 2D simulations is shown in Fig. 5.2. A timestep size of  $\Delta T = 2e - 5$ seconds was used.

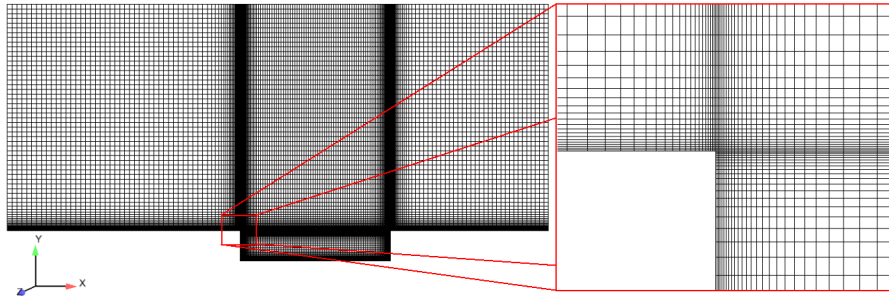


Figure 5.2: Mesh used for 2D computations with a zoomed view of mesh distribution near the leading edge of cavity

## 5.1.2 Summary of Results

Steady RANS simulations were carried out in the beginning over the same grid with different turbulence models. The SA and EARSM turbulence models exhibited similar trends, with slow convergence rate and similar flow field solution with a large recirculation region in the rear section of the cavity as shown in Fig. 5.3 and 5.4 for SA model and EARSM respectively. On the other hand SST K-omega and Wilcox turbulence models showed similar behavior with bigger oscillations in the residuals identifying the inherent unsteadiness in the flow. For both the cases convergence was not achieved. Unsteady RANS simulations were carried out for each model. It was observed that in case of Wilcox and SST k-omega model the solution could not achieve sufficient convergence in inner iterations and thus eventually diverged. On the other hand the SA and EARSM turbulence models start with periodic oscillations but go steady eventually.

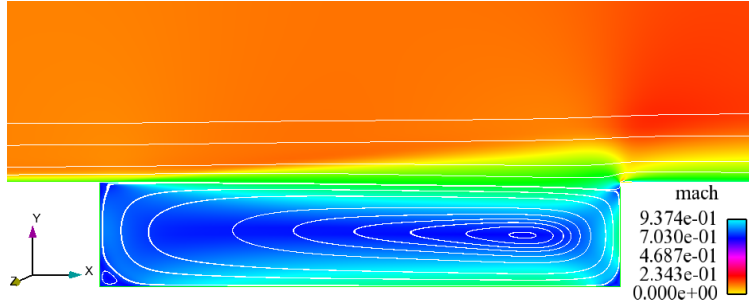


Figure 5.3: Streamlines with mach number contours on the central section  $y/W = 0$  for SA model

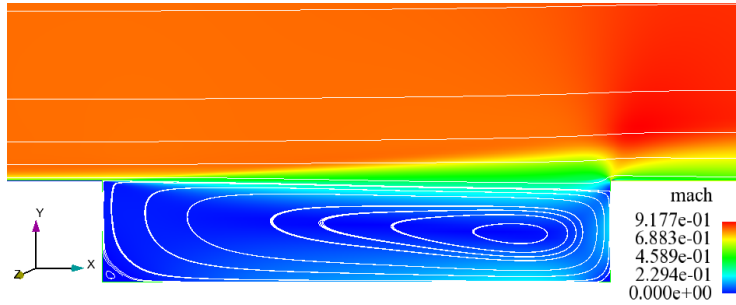


Figure 5.4: Streamlines with mach number contours on the central section  $y/W = 0$  for EARSM

## 5.2 3D Results

### 5.2.1 Mean Flow Comparison

The mean flow features were compared with the available resolved LES data by Larchevêque et al.,(2004) [28]. To begin with mean longitudinal and vertical velocity were compared at specific locations ( $x/D = 0, 0.1, 0.2, 0.3, 0.4, 0.5, 0.6, 0.7, 0.8, 0.9, 1$ ) on mid-plane of cavity ( $y = 0.0254m$ ). From Fig. 5.5 it can be seen that the DES profile matches fairly well with the LES data with some discrepancies in shearlayer close to the leading edge of the cavity, but gets better agreement with the reference data further downstreams. This can be because of the incoming boundary layer is not well resolved since we use RANS in the region close to wall and switch to LES further away from the wall. Another cause for the difference at the leading edge might be the modeled stream depletion, which is caused by mesh size and the LES region falls in the boundary layer.

In Fig. 5.6, comparison is shown between the DES and reference LES

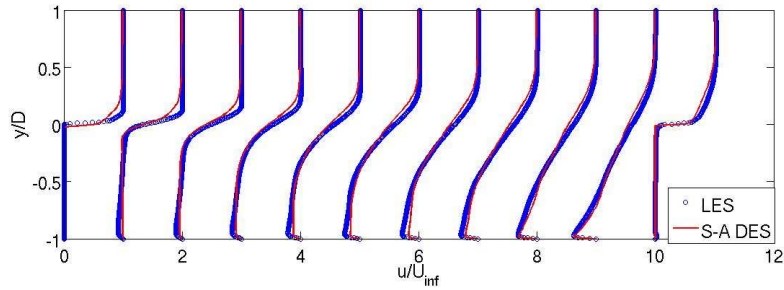


Figure 5.5: Mean streamwise velocity ( $U$ ) profile on the central section  $y/W = 0$ , in comparison with LES data [28] at specific locations over the cavity length

vertical velocity profiles, showing an obvious difference at some locations. The negative part of the profile is the indication of the deflection of the shear layer towards the cavity floor. Close to the leading edge of the cavity at  $x/L = 0.1$  the vertical velocity  $W$  is in good comparison with the LES profiles. At locations  $x/L = 0.2$  and  $0.3$  there is a slight over prediction in the positive part of the profile and further downstreams at  $x/L = 0.4, 0.5$  and  $0.6$  the  $W$  component of the velocity is under predicted showing that the strength of the large recirculation region is under predicted as compared to LES. One reason for a poor match can be the mesh resolution inside the cavity, where some part of the flow gets separated from the shear layer and give rise to a recirculation region. Close to the trailing edge of the cavity the vertical velocity and longitudinal velocity profiles matches nicely identifying that the smaller recirculation region is well captured. The shear layer predicted by DES is comparable with the LES, as the flow approaches the aft wall. This is verified by a good match between the vertical velocity (negative part of the) profile at all stations.

As discussed above the grid resolution seems not enough to resolve the shear layer, as also can be noticed in Fig. 5.7 where the shear stresses are plotted in comparison with the reference LES data, note that the last profile is at  $x/L = 0.995$ . Here we notice that the shear layer is predicted with large discrepancies specially in the first half of the cavity and also some discrepancies are observed in the recirculation region. A much better flow structure can be achieved by refining the mesh in cavity in general and shear layer in particular. Also the regions downstream where there are complex flow structures in terms of changing direction more rapidly. More specifically the kink in profile at  $x/L = 0.7$  is the location of interaction between the big and small recirculation region.

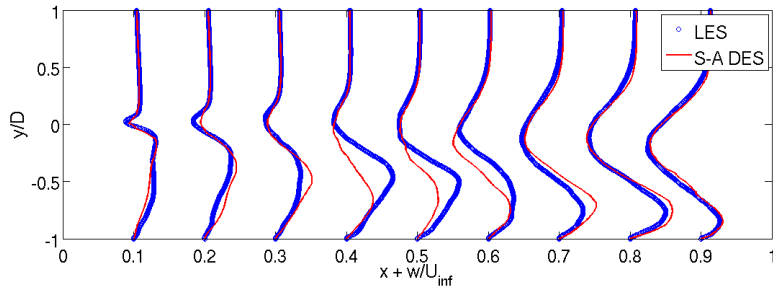


Figure 5.6: Mean vertical velocity ( $W$ ) profile on the central section  $y/W = 0$ , in comparison with LES data [28] at specific locations over the cavity length

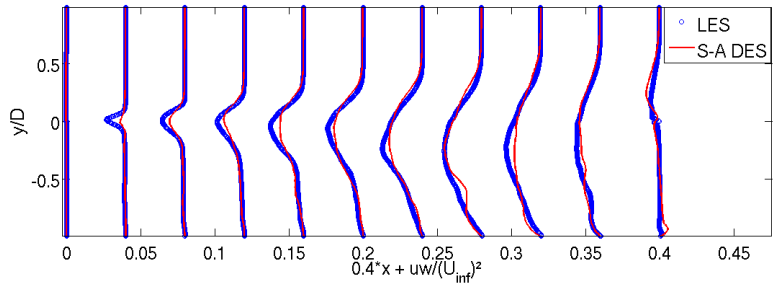


Figure 5.7: Cross Reynolds term  $\langle u'w' \rangle$  on the central section  $y/W = 0$ , in comparison with LES data [28] at specific locations over the cavity length

Resolved turbulent kinetic energy profiles are plotted at same locations as for resolved turbulent shear stresses. It can be observed in Fig. 5.8 that the turbulent structures are more energetic in the shear layer than the flow structures close to the wall. The comparison shows that the resolved turbulent shear stress is not well predicted in the shear layer closer to the leading edge until the flow reaches at  $x/L = 0.5$  where it matches more nicely and further downstream, with small discrepancies.

### Time Average mean flow features

The Fig. 5.9 shows the streamlines on the cut plane at cavity center. A large recirculation region can be observed in figure comprising of two sub-recirculation regions. A larger one is closer to the cavity center and a small one at the trailing edge and closer to the cavity floor. The mixing layer deflection can also be visualized by observing the streamlines behavior. Sufficient amount of time of 0.22 *sec* is considered for time averaging to achieve

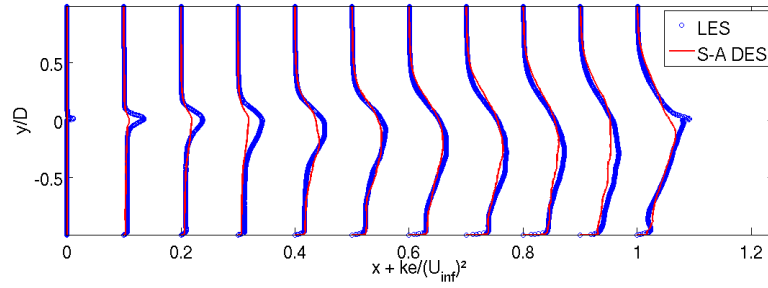


Figure 5.8: Resolved turbulent kinetic energy  $\langle K \rangle$  on the central section  $y/W = 0$ , in comparison with LES data [28] at specific locations over the cavity length

better results as identified by (reference DESider project book). The time-step size chosen is based on the observations made in the DESider project [4], suggesting that for the present cavity geometry under study a time step size of  $2e - 5$  sec or less is suitable. Velocity vectors are also plotted in cavity mid section to get a better idea about the flow field and the magnitude of the flow in different parts of the cavity and the direction. This is shown in figure 5.10.

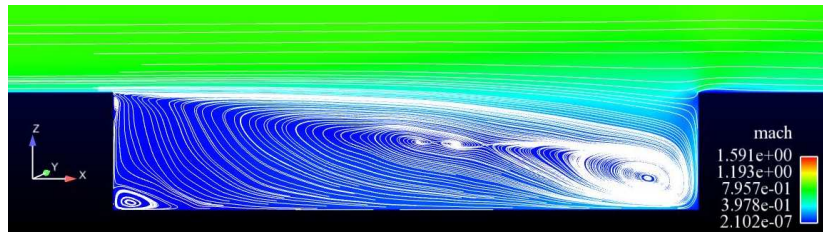


Figure 5.9: Streamlines with mach number contours on the central section  $y/W = 0$

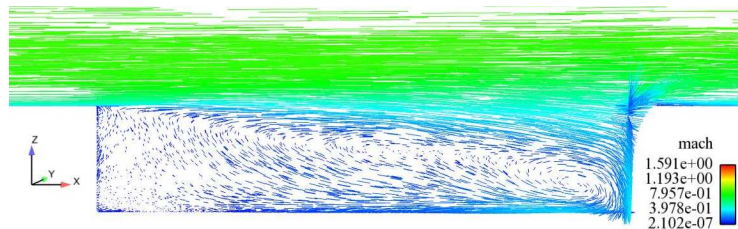


Figure 5.10: Mean velocity vectors colored with mach number on the central section  $y/W = 0$

Mean pressure distribution can be seen in Fig. 5.11. A higher pressure is observed at the rear wall of cavity with relatively sharp variation. For aeronautical applications specially store separation this is not a favorable condition, since high pressure there results in a pitching up moment of the weapon released from the weapon bay. To avoid such conditions a lot of research is being done to control the flow for example by introducing spoilers at the leading edge of the cavity to get a much uniform distribution of pressure [29].

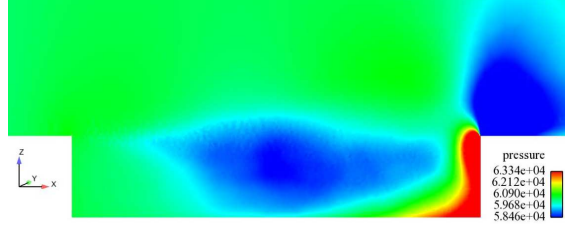


Figure 5.11: Mean pressure distribution on the cavity central section  $y/W = 0$

## 5.2.2 Pressure Oscillations

Experimental data is available for the  $M - 219$  cavity, conducted by QinetiQ, [26]. in the experiment pressure fluctuation data was recorded for the ten equally space points in x-axis direction along the cavity floor. These locations are listed down in Table 5.1 denoted as points from  $k20$  to  $k29$ . The time history of pressure fluctuations is also recorded for the DES computation for every time-step with the Nyquist frequency for sampling of  $25\text{ KHz}$  for  $0.26\text{ seconds}$ . The first  $0.04\text{ sec}$  (i.e. 2000 iterations) of the computation are discarded to avoid the transients leaving  $0.22\text{ sec}$ . The pressure fluctuation time history is transformed into Power Spectrum Density (PSD) by using Burg's method. The Sound Pressure Level (SPL) is than computed using the PSD at each location by using Eqn. 5.1

$$SPL = 20\log \left( \frac{\sqrt{PSD}}{2 \times 10^{-5}} \right) \quad (5.1)$$

The SPL for DES simulation and experimental results is plotted in Fig. 5.12 for locations  $k20$  to  $k29$  showing a reasonable match. By observing the SPL plots it can be notices that the higher frequencies (tones) magnitude is dampened unlike lower frequency modes that can be clearly identified by peaks in the plot. One of the reason for this the sampling frequency

at which the pressure fluctuations are recorded, apart from that it must be noted that the smaller structures have shorter time scales. Therefore, in case of using a larger timestep may defile these structures or not even capture them at all. This might affect the results for higher frequencies since the fast evolving structures are not well resolved. Besides these constraints, unphysical numerical diffusion might also result in dampened SPL magnitude at these higher frequencies.

<b>Kultie</b>	<b>x(inches)</b>	<b>y(inches)</b>	<b>z(inches)</b>
k20	1.0	0.0	-4.0
k21	3.0	0.0	-4.0
k22	5.0	0.0	-4.0
k23	7.0	0.0	-4.0
k24	9.0	0.0	-4.0
k25	11.0	0.0	-4.0
k26	13.0	0.0	-4.0
k27	15.0	0.0	-4.0
k28	17.0	0.0	-4.0
k29	19.0	0.0	-4.0

Table 5.1: Specified locations on cavity floor from aft wall for pressure measurement

The peaks in the SPL plots are corresponding to a discrete frequency identifying a particular mode. First four modes are identified clearly by numerical results at  $k20$  and  $k21$ . As discussed above the fourth mode corresponding to higher frequency, the SPL-magnitude is not very well resolved by the SA-DES model. Whereas, the second and third mode are clearly captured in almost all the locations. From Fig. 5.12 it can be observed that the SPL magnitude for the first mode is the least well predicted with under prediction of approximately  $2 - 7$  dB. On the other hand the second and third modes are well predicted with an under prediction ranging from less than 1-3 dB except for the third mode being slightly over predicted at  $k21$ . The fourth mode is over and under predicted in a range of  $\pm 2$  dB. The resonance frequencies for each mode are captured fairly well with a maximum difference of  $29$  Hz for fourth mode. The predicted frequencies for each mode are compare with the experimental data and Rossiter modes frequencies in Table 5.2. For the SA-DES results also a percentage difference with the experimental results is listed corresponding to each mode.

Overall Sound Pressure Level (OASPL) is also plotted on the cavity floor and compared with the experimental results available. From Fig. 5.13 it

Modes Frequency (Hz)	Mode 1	Mode 2	Mode 3	Mode 4
QinetiQ Experiment	135	350	590	820
Rossiter's Formula	148	357	566	775
SA-DES	133	376	595	849
Percentage difference between SA-DES and Experiment	1.48	7.43	0.85	3.53

Table 5.2: Comparison of frequencies for four tonal modes

can be seen that the OASPL computed by SA-DES compares well with the experimental results specially at the rear part of the cavity. OASPL is slightly over predicted with the maximum difference of magnitude less than  $1.5 \text{ dB}$ . It can be no tied that the general trend or the shape of the plot is similar to the experimental results, showing that the flow behavior over the cavity floor in terms of pressure fluctuations is similar.

Band Integrated Sound Pressure (BISPL) was also computed by filtering bands of frequencies corresponding to each Rossiter mode and than transforming it back to time domain and integrating for OASPL for each band. The frequency band ranges for each Rossiter mode have a band width of  $100 \text{ Hz}$  and spread over a range of frequencies such as to capture the peaks for both experimental and DES computations. These frequency ranges can be seen in Table 5.3. The computational results for BISPL for each mode are plotted and compared with the experimental results in Fig. 5.14. Here it can be seen that the modal shapes for each mode are well captured but with the over-prediction of magnitude by approximately  $20 \text{ dB}$  for each mode. This difference in magnitude is far more than the error observed by LES for the same geometry [28]. Same procedure was repeated at the cutplane at  $y/W = 0$ , for which a time-history was available for all the nodes after every 5 timesteps which means after every  $1e - 4 \text{ sec}$ . The mode shapes for each mode were plotted over the cutplane to identify the regions where each mode was dominant, as seen in Fig. 5.15.

Rossiter Mode	1	2	3	4
Lower limit (Hz)	100	300	550	800
Upper limit (Hz)	200	400	650	900

Table 5.3: Upper and lower limits of frequency bands for each Rossiter mode

### 5.2.3 Pressure Correlations

A better explanation or evidence is required to prove the theory behind the interaction of acoustic wave and shear layer instabilities being the source of discrete tones. For this purpose the time history for 10 points on cavity floor are used to analyze and understand the time and space dependent behavior of pressure fluctuations by computing the auto-correlation, two point time-space correlation and finally time-mode correlation.

#### Auto-correlation

The auto-correlation were computed for locations  $k21, k23, k25, k27$  and  $k29$  and compared with the experimental results. A good comparison was observed between the DES and experimental results as shown in Fig. 5.16. The time scales were computed for each location as listed in Table 5.4. Here it was noted that at the location  $k27$  the time scale was the highest with a value of  $7.593 \times 10^4 \text{ sec}$ , whereas, at other locations the auto-correlation plot are similar and approximately same time scales. One probable cause for this effect is that this is closer to the location where the larger and smaller re-circulation regions are interacting and mean flow structures with bigger time scales are transported here.

Location	k21	k23	k25	k27	k29
Time-Scale (normalized)( $\tau \times L/U_\infty$ )	56.7923	60.363	58.2	136.25	65.33

Table 5.4: Time-scale computed for pressure fluctuations at cavity floor points

Auto-correlation was also plotted for the each band of frequencies corresponding to the Rossiter modes. A more periodic behavior was observed for each mode with the increasing frequency of the cycles for higher modes. This can be seen in Fig. 5.17 where the DES correlation results are also compared with the experimental results for each mode.

#### Two Point Time-Space Correlation

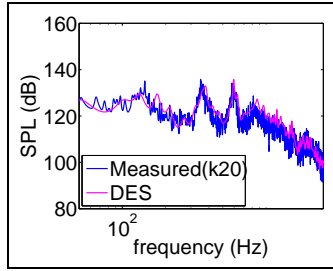
The general explanation of the relationship between the hydrodynamic and acoustic waves for cavity flow involves the hydrodynamic disturbances that travels downstream through the shear layer and ultimately impinges on the aft wall of the cavity. As a result of the interaction of the hydrodynamic

wave and cavity aft wall, acoustic waves are generated that propagates upstreams and eventually interacts with the shear layer at the cavity leading edge. Discrete tones (Rossiter modes) are created when this interaction results in resonance of either acoustic or hydrodynamic wave. The pressure measured on the cavity wall consists of disturbances of various wavelengths traveling in different directions inside the cavity. Therefore, it suggests that these pressures on cavity surface are highly correlated in specific wavelength bands. Now it is important to somehow show that these disturbances are propagating in the cavity at physically significant speeds. Therefore, two point time-space correlation is carried out and presented in Fig. 5.18. For this purpose the cavity floor points are used and two point time-space correlation are computed by keeping  $k29$  as source and moving along  $k21$ ,  $k23$ ,  $k25$  and  $k27$  and comparison is also made with the correlation plots for the experimental data.

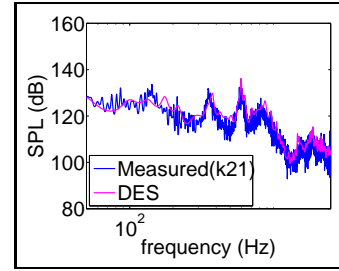
Here it must be noted that each set of correlation exhibit a cyclic behavior by showing a maximum peak followed by a periodic structure showing some resonating effects. It can be noted from Fig. 5.18 that the correlation plots does not indicate a decaying pattern of one frequency thus indicating the presence of multiple repetitive signals. Furthermore, in Fig. 5.19 the first peaks are marked with star showing the time lag between each peak, which indicates the time taken by an event when it is sensed at the other location. This is an indication of propagation of disturbances inside the cavity.

### **Time-Mode Correlation**

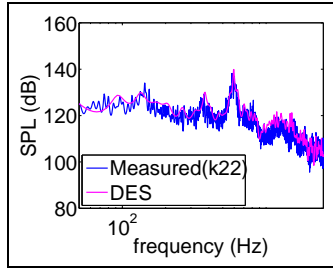
The power spectrum identified the presence of four Rossiter modes. To come up with a way to show which mode is more dominant in terms of being more correlated and therefore, causing more interaction with the cavity flow structures ( The entire signal). For this purpose the frequency bands were filtered out from the entire spectrum and transformed back from frequency domain to time domain by taking Inverse Fast Fourier Transform (ifft) in matlab. The time-mode correlation was computed between each mode and entire signal for cavity floor points. It was observed that the first mode was more correlated as compared to the rest of the modes. This was expected since the hydrodynamic waves are not accompanied with high frequencies. Therefore, the first mode being low frequency had a better correlation. As the frequency is increased the correlation coefficient magnitude is reduced as shown in Fig. 5.20.



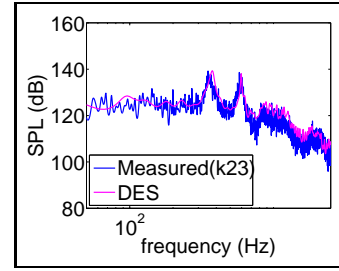
(a) k20



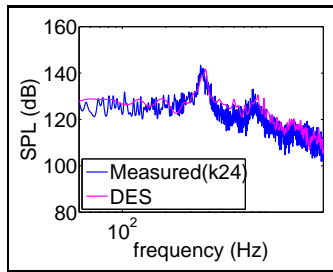
(b) k21



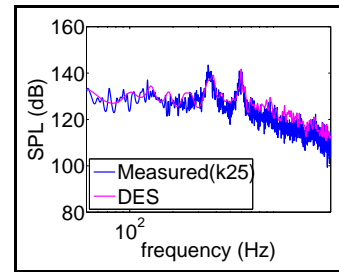
(c) k22



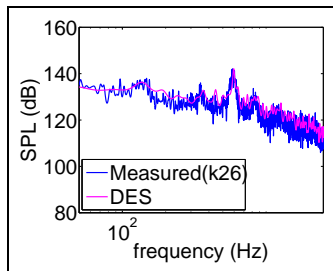
(d) k23



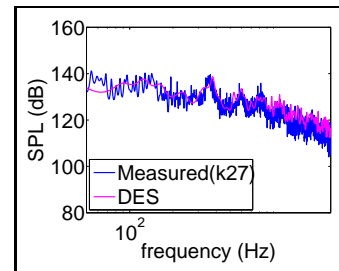
(e) k24



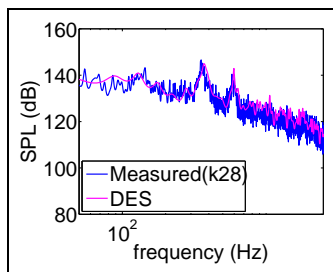
(f) k25



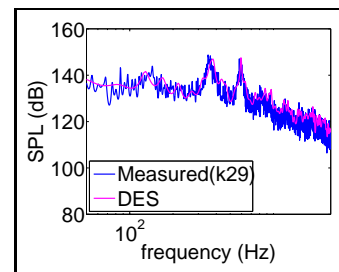
(g) k26



(h) k27



(i) k28



(j) k29

Figure 5.12: Comparison of SPL at locations from  $k20$  to  $k29$  on cavity floor

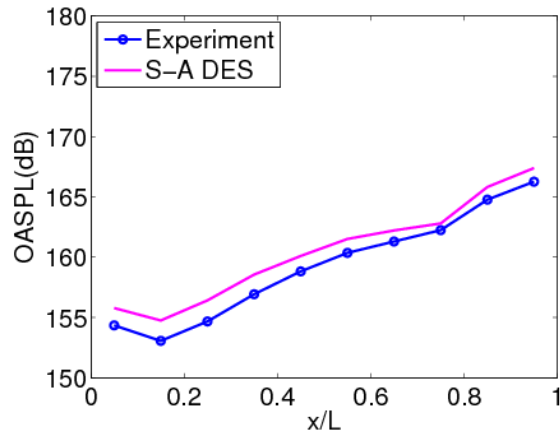


Figure 5.13: OASPL plotted on the cavity central section  $y/W = 0$  at locations  $k20$  to  $k29$

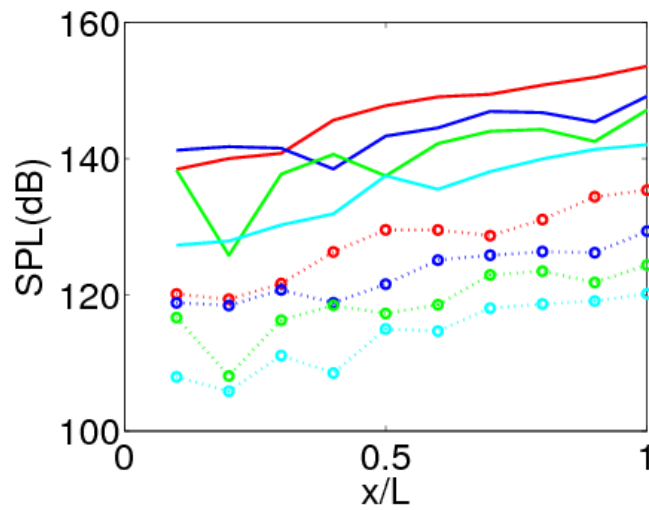
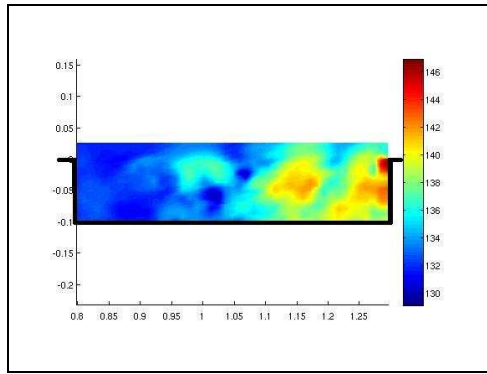
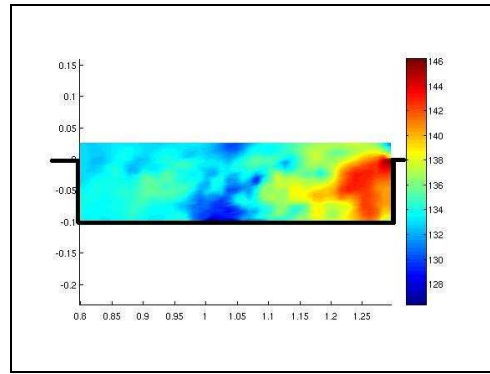


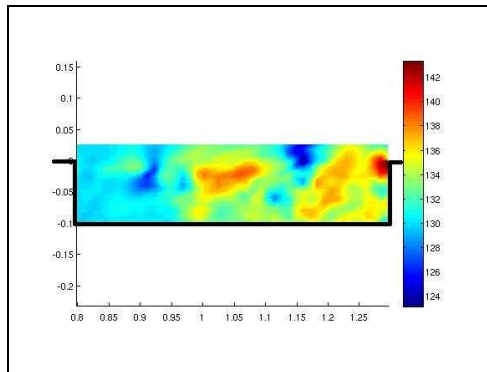
Figure 5.14: Streamwise evaluated Band-Integrated Sound Pressure Level (BISPL) plotted on the cavity central section  $y/W = 0$  at locations  $k20$  to  $k29$ , mode 1-red, mode 2-blue, mode 3-green, mode 4-cyan. DES(solid), EXP(dotted)



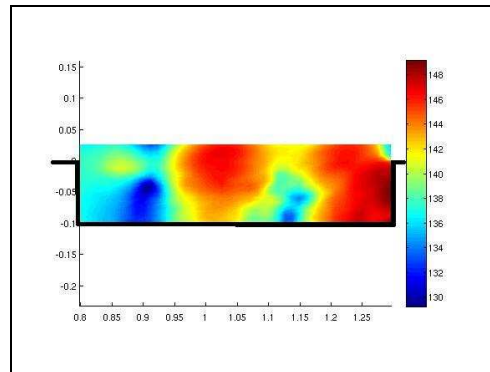
(a) Mode 1



(b) Mode 2

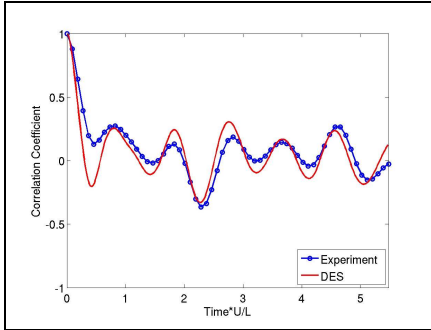


(c) Mode 3

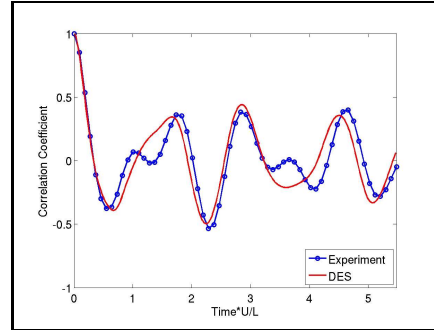


(d) Mode 4

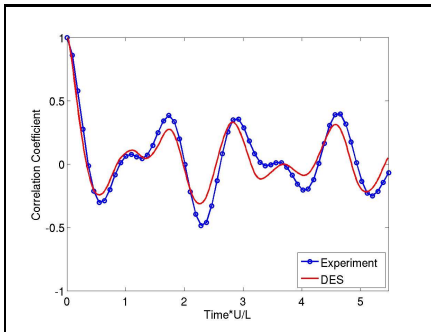
Figure 5.15: Band Integrated sound pressure level (BISPL) at the cavity mid-section for each mode



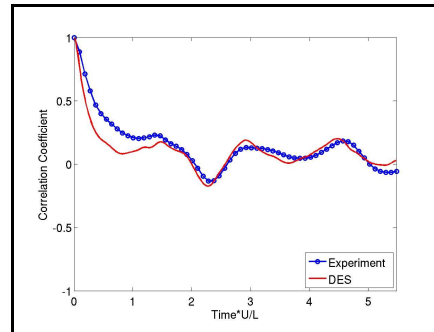
(a)  $k_{21}$



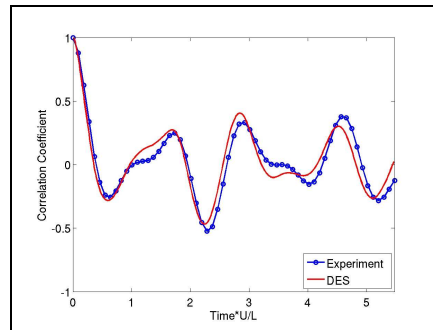
(b)  $k_{23}$



(c)  $k_{25}$

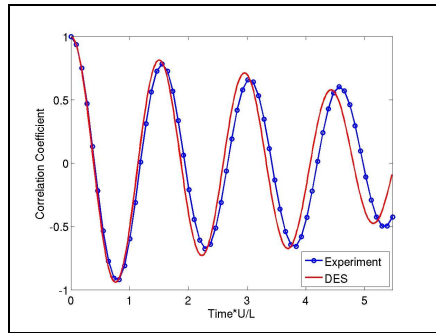


(d)  $k_{27}$

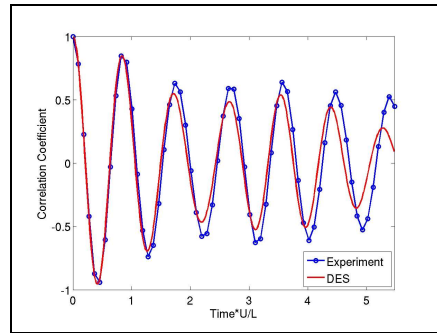


(e)  $k_{29}$

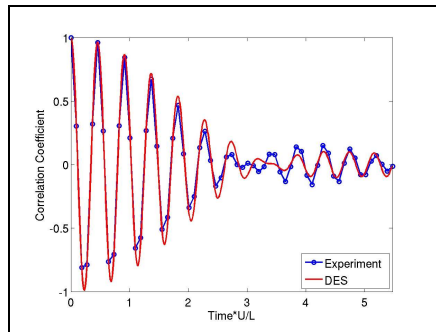
Figure 5.16: Auto-correlation plots for locations  $k_{21}$ ,  $k_{23}$ ,  $k_{25}$ ,  $k_{27}$  and  $k_{29}$  on cavity floor



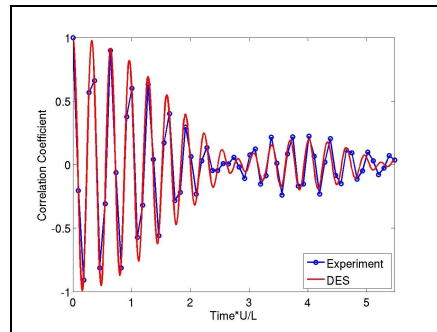
(a) Mode 1



(b) Mode 2



(c) Mode 3



(d) Mode 4

Figure 5.17: Auto-correlation plots for frequency band corresponding to Rossiter modes at locations  $k29$  on cavity floor

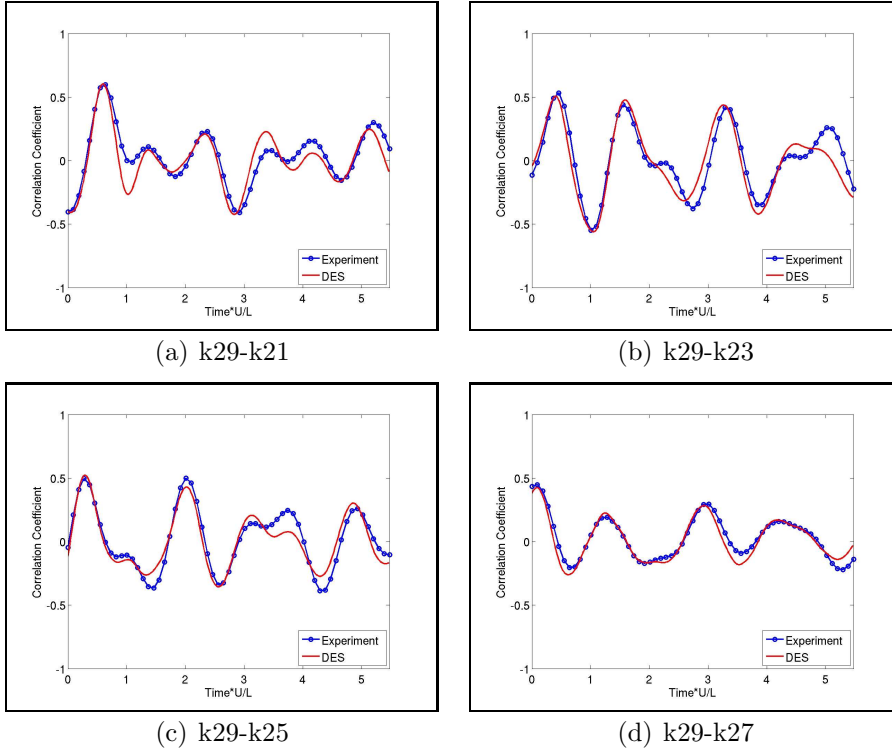


Figure 5.18: Time-Space Correlation with  $k_{29}$  as source with  $k_{21}$ ,  $k_{23}$ ,  $k_{25}$  and  $k_{27}$  compared with the Experimental results

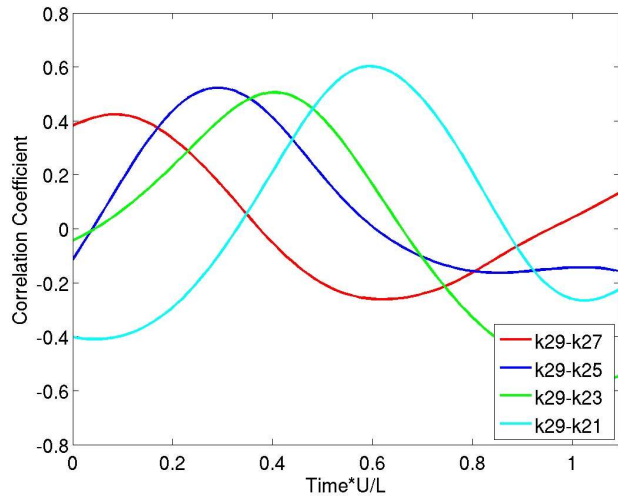


Figure 5.19: Time-Space Correlation with  $k_{29}$  as source with  $k_{21}$ ,  $k_{23}$ ,  $k_{25}$  and  $k_{27}$

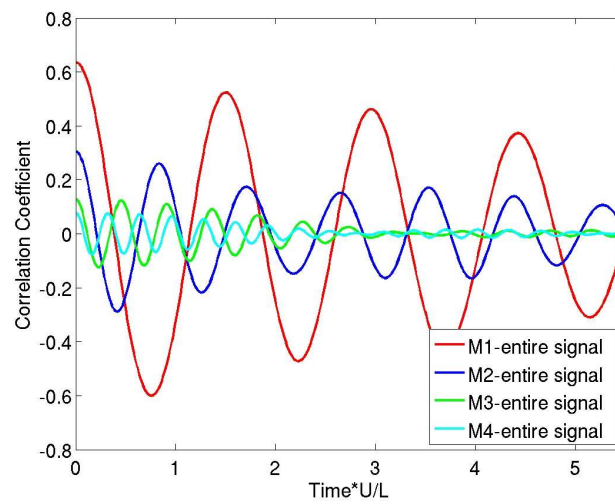


Figure 5.20: Time-Mode Correlation (at k29) plotted for frequency band of each Rossiter mode with entire signal'

# Chapter 6

## Conclusion and Outlook

### 6.1 Conclusion and Outlook

The SA-DES turbulence model is used to simulate a high Reynolds number flow over a three-dimensional cavity. The computational results are validated by comparison with the available experimental and LES data. The predicted pressure fluctuations are compared with the experimental data available. Whereas, time-averaged mean flow features are compared with the available LES results. In general the instantaneous as well as the mean flow features were reasonably well resolved by SA-DES.

The pressure fluctuations were analyzed by computing sound pressure level (SPL) where the four tonal modes were also revealed as peaks in the spectrum. The frequencies corresponding to these modes were independent of the location over the cavity length. The second and third mode were more dominant as they were clearly captured at almost every location. The DES computation did not produce the fourth mode well as at some locations peak was smeared. The overall sound pressure level calculated from DES gives a reasonable agreement with the experiment, more specifically in the second half of the cavity. The mean flow features observed in DES computation agreed well with the benchmark LES findings. However in the recirculation region there are some discrepancies clearly visible from the mean vertical velocity plots. The incoming boundary layer is not very well resolved by SA-DES as compared to the LES, this is indicated in the mean streamwise velocity profile close to the leading edge of the cavity.

A cyclic behavior of the time-space correlation without decaying in magnitude of correlation coefficient shows that multiple wavelength waves are traveling in different directions in the cavity. The first mode is more correlated to the entire signal as compared to the higher frequency modes. The

correlation magnitude reduces as we move to higher frequency modes as indicated by the time-mode correlation plots.

The results seem motivating specially the correlation analysis. In future efforts can be made to store the data for entire domain at each time step and the pressure correlation analysis can be carried out to get a more accurate insight into the shear layer. Better filtering techniques can be applied to filter out the signal noise while studying frequency bands for each mode.

# Bibliography

- [1] A. Roshko. Some measurements of flow in a rectangular cutout. Technical note - 3488, National Advisory Committee for Aeronautics, Washington, USA, 1955.
- [2] T. Colonius C. W. Rowley and A. J. Basu. On self-sustained oscillations in two-dimensional compressible flow over rectangular cavities. *J. Fluid Mech.*, 455:315–346, 2002.
- [3] J. E. Rossiter. Wind-tunnel experiments on the flow over rectangular cavities at subsonic and transonic speeds. Reports and memoranda 3438, Aeronautical Research Council, 1964.
- [4] S.-H. Peng. Application - Test Cases: M219 cavity flow. In *DESider - A European Effort on Hybrid RANS-LES Modelling*, volume 103 of *Notes on Numerical Fluid Mechanics and Multidisciplinary Design*, pages 270–285. Springer Verlag, 2007.
- [5] N. Toy P. J. Dismile and E. Savory. Effect of planform aspect ratio on flow oscillations in rectangular cavities. *Trans. ASME: J of Fluids Engineering.*, 122:32–38, 2000.
- [6] K. K. Ahuja and J. Mendoza. Effects of cavity dimensions, boundary layer, and temperature on cavity noise with emphasis on benchmark data to validate computational aeroacoustic codes. Contractor report 4653, NASA, 1995.
- [7] S. T. Bjorge. Flow around an object projected from a cavity into a supersonic freestream. Msc thesis, Department of the Air Force Air University, Air Force Institute of Technology, Wright-Patterson Air Force Base, Ohio, USA, 2004.
- [8] D. M. Bortz et al. Reduced order modelling in control of open cavity acoustics. Technical report a820454, Center for Research in Scientific

Computation, North Carolina State University, Raleigh, North Carolina, USA, 2000.

- [9] S.Garg M. Kegerise, E. Spina and L. Cattafesta. Mode-switching and nonlinear effects in compressible flow over a cavity. *Physics of Fluids*, 16(3):678–687, 2004.
- [10] P. J. W. Block. Noise response of cavities of varying dimensions at subsonic speeds. Technical note d-8351, NASA, 1976.
- [11] M. B. Tracy and E. B. Plentovich. Characterization of cavity flow fields using pressure data obtained in the langley 0.3-meter transonic cryogenic tunnel. Technical memorandum 4436, NASA, Langley Research Center, Hampton, Virginia, USA, 2004.
- [12] A. J. Basu T. Colonius and C. W. Rowley. Numerical investigation of the flow past a cavity. In *AIAA Paper 99-1912, 5th AIAA/CEAS Aeroacoustics Conference*, May, Bellevue, Washington, USA, 1999.
- [13] L. L. Shaw R. S. Gates, C. Butler and R.E. Dix. Aeroacoustic effects of body blockage in cavity flow. In *AIAA Paper 87-2667, 11th AIAA Aeroacoustics Conference*, 19-21 Oct, Sunnyvale, California, USA, 1987.
- [14] V. Sarohia and P.E. Massier. Control of cavity noise. *Journal of Aircraft*, 14:833–837, 1977.
- [15] D. Rockwell and E. Naudascher. Review - self-sustaining engineering applications of computational fluid mechanics oscillations of flow past cavities. *Journal of Fluids Engineering*, 100:152–165, 1978.
- [16] P.R. Spalart, W.-H. Jou, M. Strelets, and S.R. Allmaras. Comments on the feasibility of LES for wings and on a hybrid RANS/LES approach. In C. Liu and Z. Liu, editors, *Advances in LES/DNS, First Int. conf. on DNS/LES*, Louisiana Tech University, 1997. Greyden Press.
- [17] P. R. Spalart and S. R. Allmaras. A one-equation turbulence model for aerodynamic flow. *Larecherche aerospatale*, 1:5–21, 1994.
- [18] C. David Wilcox. Reassessment of the scale-determining equation for advanced turbulence model. *AIAA Journal*, 26:1299–1310, 1988.
- [19] F. R. Menter. Two-equation eddy-viscosity turbulence models for engineering applications. *AIAA Journal*, 32:1598–1605, 1994.

- [20] Stefan Wallin and Arne V. Johansson. An explicit algebraic reynolds stress model for incompressible and compressible turbulent flows. *Journal of Fluid Mechanics*, 403:89 – 132, 2000.
- [21] Stefan Wallin and Arne V. Johansson. Modelling streamline curvature effects in explicit algebraic reynolds stress turbulence models. *International Journal of Heat and Fluid Flow*, 23:721 – 730, 2002.
- [22] A. Hellsten. New advanced k-omega turbulence model for high-lift aerodynamics. *AIAA Journal*, 43:1857 – 1869, 2005.
- [23] FOI. Edge user guide. User manual, foi dnr 03-2879, Defense and Security, Systems and Technology, FOI, Swedish Defense Research Agency, Stockholm, Sweden, 2007.
- [24] FOI. Edge theoretical formulation. User manual, foi dnr 03-2879, Defense and Security, Systems and Technology, FOI, Swedish Defense Research Agency, Stockholm, Sweden, 2007.
- [25] Q. Abbas and J. Nordström. Weak versus. strong no-slip boundary conditions for the navier stokes equations. *Engineering Applications of Computational Fluid Mechanics*, 4:29–38, 2010.
- [26] M. Henshaw and J. de Charentenay. In verification and validation data for computational unsteady aerodynamics. Technical report rto-tr-26, ac/323(avt)tp/19, QinetiQ, British Aerospace (Operations) Ltd., Military Aircraft and Aerostructures Skillings Lane, Brough, East Riding of Yorkshire, HU151EQ U.K., 2002.
- [27] S. H. Peng and S. Leicher. Des and hybrid rans-les modelling of unsteady pressure oscillations and flow features in a rectangular cavity. *S. -H. Peng., W. Haase, Advances in Hybrid RANS-LES Modelling. Notes on Numerical Fluid Mechanics and Multidisciplinary Design*, 97:132–141, 2008.
- [28] T.-H. Le L. Larchevêque, P. Sagaut and P-Comte. Large-eddy simulation of a compressible flow in a three-dimensional open cavity at high reynolds number. *Journal of Fluid Mechanics*, 516:265–301, 2004.
- [29] M. Mallet V-Levasseur, P. Sagaut and F. Chalot. Unstructured large eddy simulation of the passive control of the flow in a weapon bay. *Journal of Fluids and Structures*, 24:1204–1215, 2008.